Computational Mechanics manuscript No.
(will be inserted by the editor)

Multiscale modelling framework for the fracture of thin brittle polycrystalline films - Application to polysilicon

Shantanu S. Mulay · Gauthier Becker · Renaud Vayrette · Jean-Pierre Raskin · Thomas Pardoen · Montserrat Galceran · Stéphane Godet · Ludovic Noels

Received: date / Accepted: date

Abstract Micro-electro-mechanical systems (MEMS) made of polycrystalline silicon are widely used in several engineering fields. The fracture properties of polycrystalline silicon directly affect their reliability. The effect of the orientation of grains on the fracture behaviour of polycrystalline silicon is investigated out of the several factors. This is achieved, firstly, by identifying the statistical variation of the fracture strength and critical strain energy release rate, at the nanoscopic scale, over a thin freestanding polycrystalline silicon film, having mesoscopic scale dimensions. The fracture stress and strain at the mesoscopic level are found to be closely matching with uniaxial tension experimental results. Secondly, the polycrystalline silicon film is considered at the continuum MEMS scale, and its fracture behaviour is studied by incorporating the nanoscopic scale effect of grain orientation. The entire modelling and simulation of the thin film is achieved by combining the discontinuous Galerkin method and extrinsic cohesive law describing the fracture process.

Shantanu S. Mulay, Ludovic Noels
University of Liege, Department of Aerospace and Mechanical Engineering, Computational & Multiscale Mechanics of Materials, Chemin des Chevreuils 1, B-4000 Liège, Belgium. Tel.: +32-43669503
E-mail: ssmulay@ae.iitm.ac.in, E-mail: L.Noels@ulg.ac.be

Gauthier Becker
Massachusetts Institute of Technology, Department of Aeronautics and Astronautics, 77, Massachusetts Avenue, Cambridge, MA 02139-4307, United States

Renaud Vayrette, Jean-Pierre Raskin, Thomas Pardoen
Université catholique de Louvain, Institute of Mechanics, Materials and Civil Engineering, Place Sainte Barbe 2, 1348 Louvain-la-Neuve, Belgium.

Montserrat Galceran
CIC Energigune, Albert Einstein 48, 01510 Miñano (Álava), Spain

Stéphane Godet
Université Libre de Bruxelles, Materials Engineering, characterization, synthesis and recycling,
50 Av. FD Roosevelt CP194/03, 1050 Brussels, Belgium.

Keywords polysilicon fracture · Discontinuous Galerkin method · multiscale framework · MEMS fracture

1 Introduction

Polycrystalline silicon (polySi) is the most common material in use for the manufacturing of MEMS. However, several factors, such as the grain size, grain orientation, and nano scale defects or flaws, affect the mechanical properties of thin polySi films, such as the Young's modulus E, fracture strength σ_c, and critical energy release rate G_c [1]. Apart from this, a specific manufacturing process adopted to produce MEMS also further affects the run-time fracture behaviour of MEMS. There is thus a need to develop numerical models accounting for these probabilistic nano-scale effects to predict the properties, including the strength, of MEMS components.

It is pertinent at first to clearly define the relevant length scales to illustrate the problem addressed in the present work. The length dimension ranging from 1 nm to 100 nm is referred as the nanoscopic scale, from 100 nm (0.1 μm) to 1000 nm (1.0 μm) is referred as the mesoscopic or microscopic scale, and higher than 1.0 μm is referred as the MEMS or macroscopic scale. Thus, an average single grain size of polySi ($\approx$ 100 nm) falls under the nanoscopic scale, the size of the simulation model of a thin polySi film consisting of several grains fall under the mesoscopic or microscopic scale (size of representative or microstructural volume element), and finally the size of the simulation model of a thin polySi film having a continuum structure, i.e., without the explicit representation of the underlying micro-structure, falls under the macroscopic length scale. The length scales

will be correspondingly referred in the subsequent sections of this paper.

Several advanced techniques based on micro-mechanical tests [2, 3] have been developed over the years to correctly measure the mechanical properties E, σ_c, and G_c of a bulk polySi and single crystal silicon presenting a preferred out of plane orientation, such as <1 0 0> or <1 1 0> or <1 1 1>, involving the statistical aspects. These researches report some variations in the mean values of E and σ_c at both, the micro and macroscopic levels. This could be explained by the random orientation of grains at the mesoscopic level leading to a statistical strength distribution at the macroscopic level, and thus two samples may have completely different crack paths (trans-granular or inter-granular) as well as different fracture strengths. The literature also reports a decrease of the fracture strength with respect to an increase in the thickness of the test sample [4]. This could be explained by the presence of more surface flaws across the thickness in the thicker specimens. The presence of wanted or unwanted foreign elements in the polySi can also have a first order effect on the fracture strength. Thus all these reasons warrant a robust design procedure of MEMS, made up of polySi, linking the probabilistic nature of the fracture behaviour of polySi at the mesoscopic level with the macroscopic level.

The fracture of a thin polySi film involves the nanoscopic scale corresponding to the grain size, as well as the macroscopic scale corresponding to the specimen dimensions. The fracture properties (σ_c, G_c and crack path) of polySi vary at the nanoscopic scale due to the several factors mentioned earlier. Therefore, the prediction of the fracture behaviour at the MEMS scale is a particularly challenging task as it strongly depends on the lower scale effects. One of the primary motivations behind this study is that the finite element size of the discretized micro-structure is constrained by the smallest grain size present in the model. Indeed, a large number of elements, varying in size, are generated even for a fewer number of grains in a model of the polySi film. Therefore, very small load increments are required in order to achieve a stable quasi-static simulation. In fact, an average grain size of approximately 100 nm leads to a time step around $\approx 1 \times e^{-15}$ sec., resulting in an unaffordable computational time even within a scalable parallel implementation, and preventing the direct numerical simulation of polycrystalline MEMS structures. This problem requires to be addressed using 2-scale methods in order to have a much larger finite element size at the macroscopic length.

Different techniques have been proposed in the literature to account for a lower scale when simulating the fracture process. Multi-scale computational homogenization (or FE^2) methods separate the resolution at the two scales, allowing to keep coarse meshes at the higher scale where a macro-crack is introduced at the expense of the concurrent resolution of many micro-scale problems. However computational multiscale fracture mechanics remains challenging, mainly because discontinuities have to be propagated through the different scales. One problem linked to this propagation is the loss of representative nature of the micro-problem [5–7]. This can be solved by using appropriate boundary conditions [5], with the concept of failure zone averaging [6], for periodic structures [7], or by propagating the discontinuities to the macro-level by characterizing the loss of ellipticity at the sub-scale [8]. In [9], the reaction forces of the micro-scale boundary value problem, which embeds crack propagation, are used to characterize the fracture properties of a crack at the macro-scale. Clearly the concurrent resolution of the multiple non-linear micro-scale problems with the non-linear macro-scale problem induces prohibitive costs. A multi-resolution strategy using a combination of a damage model and of a generalized micro-continuum has recently been proposed to capture zig-zag fracture of heterogeneous ductile materials [10, 11]. This multi-resolution method requires an increase of the number of degrees of freedom but the two scales are solved at once. In [12] a reduced order modelling technique based on the domain partitioning method was used to refine locally the discretization in the zones of damage evolution. Finally the evolution of micro-scale cracks was accounted for at the macro-scale by using the projection method [13].

In this work we intend to take advantage of the brittle behaviour of the material by replacing the concurrent resolution of the two scales by statistical mesoscopic fracture properties, while solving an unmodified macro-scale problem. To this end, finite element simulations of the microstructure, explicitly modelling the different grains, are conducted from which the statistical mesoscopic fracture properties can be extracted following the method described in [9, 14] to feed the finite element simulation of the MEMS structure on which scale the grains are thus implicitly modelled. The main objective is to link the effect of the grains orientation at the nanoscopic level to the fracture of MEMS at the macroscopic level to contribute to more robust design tools.

At both the mesoscopic and macroscopic levels, the finite element simulations, accounting for the fracture process of a thin polySi film, have recourse to the cohesive zone method (CZM). The CZM considers a cohesive zone (process zone) ahead of the crack tip, such that the force on the crack lips within the cohesive zone progressively vanishes, leading to a fully open crack [15, 16]. The total energy released per unit of the newly created crack surface area (J/m^2) during the crack opening is equal to the fracture energy or critical strain energy release rate G_c. The CZM has extensively be used in fracture mechanics. The cohesive zone can be integrated using the extended finite element method (xFEM) [17, 18], the embedded localization method (EFEM) [19], or with interface elements inserted between

the usual bulk finite elements. For the two first approaches, the crack can be represented in an arbitrary existing FE mesh through global or local enrichments [20]. When having recourse to cohesive elements, the CZM can be implemented, on the one hand, using intrinsic cohesive laws (ICLs) modelling the elastic response prior to the fracture onset [21] or, on the other hand, using extrinsic cohesive laws (ECLs) inserted in the model at the fracture onset only [22, 23]. Intrinsic laws have been firstly preferred to extrinsic ones due to their easier implementation. Nevertheless, intrinsic cohesive laws lead to an inconsistent pure penalty method. On the contrary, ECLs preserve the consistency but they are more complicated to implement in the case of continuous Galerkin methods as some topological mesh modifications are required during the simulation.

To avoid these topological mesh modifications, in this work we consider the combination of the extrinsic cohesive laws to the discontinuous Galerkin (DG) method to integrate the CZM. The DG method takes into account the discontinuities (jumps) in the field variable distribution within the interior of the problem domain, and the ECL approach performs the unloading of the force on the newly created fracture surfaces. The weak form of the DG method is developed similarly to the classical finite element method (FEM), except that the boundary integral terms do not vanish, e.g. [24]. The integration by parts is restricted to the sub-domains, thus the boundary integral terms arising from it across the sub-domain boundaries are retained and used to capture the discontinuities across the element interfaces. This makes it suitable to integrate the ECL upon the onset of fracture since the interface elements are present before the insertion of the cohesive element, as in the intrinsic approach [25]. Nonetheless, contrarily to the pure penalty intrinsic method, the DG-/ECL framework ensures the consistency of the method by adequate flux terms at the interfaces. The detailed discussion and formulation of the DG/ECL method can be found in the references [26] for 3D formulations while [27,28] discussed DG shell formulations. The DG/ECL method offers important advantages. Indeed, besides being consistent and ensuring convergence with respect to the mesh size, the method does not require complex modifications of the FE code, including in the 3D parallel case, as recently discussed in the cases of in-house and commercial software [29, 30]. Moreover, the method remains scalable for a high number of processors (a few thousands [26]), ensuring its computational efficiency. Finally the DG/ECL method does not require criteria for cracks bifurcation, merge and propagation direction, allowing for multiple cracks to propagate and interact in the structures.

Firstly, the fracture of freestanding polySi thin films is simulated at the mesoscopic level by meshing explicitly several grains present in the RVE. A plane-stress 2-D assumption is made, reducing the computational cost since there is no explicit discretization across the film thickness. The values of σ_c and G_c at the nanoscale are experimentally available for a single crystal silicon with preferred out of plane grain orientations $<1\,0\,0>, <1\,1\,0>$ and $<1\,1\,1>$. However, with finite element simulations the crack direction is constrained by the element boundaries, which are not aligned with these particular planes. A new formulation is thus proposed that computes the effective values of σ_c and G_c for an arbitrary orientation of the crack from the three reference values. Furthermore, several grains are experimentally observed over the thickness of a thin polySi film [3,31–33]. For these reasons the fracture path is not perpendicular to the MEMS surface and is not uniform across the thickness. Even in the case of a single grain across the thickness, the fracture surface does not necessarily remain perpendicular to the film surface as a weaker plane can exist. Thus the thickness of a thin polySi film is implicitly considered in our 2D plane-stress simulations while identifying the weakest fracture plane for the through-the-thickness fracture. These simulation results (fracture strength and strain) are compared with corresponding experiments. In the experiments, the films have been tested freestanding by etching the underneath sacrificial layer [34–39] so that they undergo pure uniaxial tension conditions. A plane-stress condition in thus considered in the 2D-numerical simulations. Moreover in this considered experimental setup, the fracture of the polySi film does not interact with the substrate.

Several sets of the micro-structure simulation results can thus be obtained by assigning each time, a random orientation to the grains. A mesoscopic cohesive law is then extracted for each set of results [9, 14], and the mean and standard deviation values of σ_c and of the maximum crack tip opening displacement are computed. An average mesoscopic cohesive law is then developed based on these values. The fracture of a polySi thin film can then be performed at the macroscopic level using this average cohesive law, for a much larger model without the explicit representation of the underlying micro-structure.

This paper is organised as follows. The formulations of both DG and ECL methods are given in Section 2. The description of the micro-model, including the formulations to account for a general orientation of crack direction and for the effect of the thickness of polySi thin film is reported in Section 3. This Section also reports the extraction of statistical mesoscopic cohesive law using this micro-model and the comparison with experimental data. The fracture studies of a thin polySi film is thus performed at the macroscale in Section 4. The conclusions are finally drawn in Section 5.

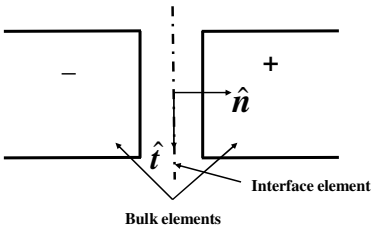

Fig. 1: Interface element with local basis vectors in-between the two 2D bulk elements, "minus" and "plus", in the DG method

2 Discontinuous Galerkin method and extrinsic cohesive law framework

In this section, the DG/ECL framework of the weak formulation accounting for fracture is summarised as well as the constitutive bulk and cohesive model behaviours.

2.1 Weak formulation

The thin polySi film is first treated as a continuum at the mesoscopic level with a discretization of the grains, and then at the macroscopic level with homogenised properties, following the DG method and assuming small deformations.

Let $\Omega \subset \mathbf{R}^2$ be a body subjected to a force per unit mass $\boldsymbol{b}$ (N/Kg). Its boundary surface Γ includes two parts: the Dirichlet boundary denoted by Γ_{D}, where the displacement $\boldsymbol{u}$ is prescribed by $\bar{\boldsymbol{u}}$, and the Neumann boundary denoted by Γ_{T}, where the traction is prescribed by $\bar{\boldsymbol{t}}$. One always has $\Gamma = \Gamma_{\mathrm{D}} \cup \Gamma_{\mathrm{T}}$ and $\Gamma_{\mathrm{D}} \cap \Gamma_{\mathrm{T}} = \emptyset$. The continuum mechanical equilibrium equations in the material form are stated as

$$\nabla \cdot \boldsymbol{\sigma}^{\mathrm{T}} + \rho\, \boldsymbol{b} = \rho\, \ddot{\boldsymbol{u}} \quad \text{in } \Omega \tag{1}$$

$$\boldsymbol{u} = \bar{\boldsymbol{u}} \quad \text{on } \Gamma_{\mathrm{D}} \text{ and} \tag{2}$$

$$\boldsymbol{\sigma}\hat{\boldsymbol{n}} = \bar{\boldsymbol{t}} \quad \text{on } \Gamma_{\mathrm{T}} \tag{3}$$

where ρ is the density, $\boldsymbol{\sigma}$ is the Cauchy stress tensor, and $\hat{\boldsymbol{n}}$ is the outward normal to the unit surface in the current configuration.

The 2D finite element discretization of the body Ω is expressed as $\Omega = \bigcup_e \bar{\Omega}^e$, where $\bar{\Omega}^e$ is the union of the open domain Ω^e with its boundary Γ^e. Here the symbol Ω is used to represent the whole body and its discretization for simplicity. The mesh of the geometry contains bulk elements and all the boundaries in-between them are treated as interface elements, as shown in Figure 1. The weak form of Equations (1-3) arises by seeking a polynomial approximation $\boldsymbol{u}$ of the displacement field over the discretization Ω. Contrarily to a continuous Galerkin approximation, which requires $\boldsymbol{u} \in C^0(\Omega)$, the DG approach requires only an element–wise continuous polynomial approximation, *i.e.*, $\boldsymbol{u} \in C^0(\Omega^e)$. Consequently, for a DG formulation the trial functions $\boldsymbol{w}_u$ are also discontinuous across the element interfaces on the internal boundary of the body $\Gamma_{\mathrm{I}} = [\bigcup_e \Gamma^e] \setminus \Gamma$.

The new weak formulation of the problem is obtained in a similar way as for the continuous Galerkin approximation. The linear momentum balance is enforced in a weighted average sense by multiplying the strong form (1) by a suitable trial function $\boldsymbol{w}_u$ and by integrating by parts in the domain. However, since both test and trial functions are discontinuous, the integration by parts is not performed over the whole domain but on each element instead. Using established DG considerations, see [24] for details, this leads to

$$\left.\begin{aligned} \int_\Omega (\rho\, \ddot{\boldsymbol{u}} \cdot \boldsymbol{w}_u + \boldsymbol{\sigma} : \nabla \boldsymbol{w}_u)\, dv + \int_{\Gamma_{\mathrm{I}}} [\![\boldsymbol{w}_u]\!] \cdot \langle \boldsymbol{\sigma} \rangle \cdot \hat{\boldsymbol{n}}^-\, ds \\ = \int_\Omega \rho\, \boldsymbol{b} \cdot \boldsymbol{w}_u\, dv + \int_{\Gamma_{\mathrm{T}}} \boldsymbol{w}_u \cdot \bar{\boldsymbol{t}}\, ds \end{aligned}\right\} \tag{4}$$

where $\hat{\boldsymbol{n}}^-$ is the outward normal to the unit surface of the "minus" element on one side of the interface. The Equation (4) contains all the usual terms from the classical Galerkin method with an extra terms accounting for the discontinuities of the field at inter element boundaries. In this equation we have considered the jump and average operators, which are defined on an interface of two bulk elements of the discretized geometry, arbitrarily denoted "plus" and "minus" as shown in Figure 1, respectively, as

$$[\![\bullet]\!] = \left[\bullet^+ - \bullet^-\right] \quad \text{and} \quad \langle \bullet \rangle = \frac{1}{2}\left[\bullet^+ + \bullet^-\right] \tag{5}$$

In the formulation (4) so far, neither the displacement continuity in-between the elements, nor the stability of the method are enforced. Moreover one should account for the interfaces Γ_{IU} corresponding to uncracked surfaces, and for the interfaces Γ_{IC} corresponding to cracked surfaces, with $\Gamma_{\mathrm{IC}} \cup \Gamma_{\mathrm{IU}} = \Gamma_{\mathrm{I}}$.

On cracked surfaces Γ_{IC}, the surface traction $\langle \boldsymbol{\sigma} \rangle \cdot \hat{\boldsymbol{n}}^-$ arises from a cohesive zone model and reads $\bar{\boldsymbol{t}}^-([\![\boldsymbol{u}]\!])$, yielding

$$\int_{\Gamma_{\mathrm{IC}}} [\![\boldsymbol{w}_u]\!] \cdot \langle \boldsymbol{\sigma} \rangle \cdot \hat{\boldsymbol{n}}^-\, ds = \int_{\Gamma_{\mathrm{IC}}} [\![\boldsymbol{w}_u]\!] \cdot \bar{\boldsymbol{t}}^-([\![\boldsymbol{u}]\!])\, ds \tag{6}$$

On uncracked surfaces Γ_{UC}, the compatibility equation $\boldsymbol{u}^+ - \boldsymbol{u}^- = 0$ is enforced through a so–called symmetrization term in $[\![\boldsymbol{u}]\!]$ and a (sufficiently large) quadratic stabilisation term in $[\![\boldsymbol{u}]\!]$ and $[\![\boldsymbol{w}_u]\!]$. We thus use the classical substitution inherent to consistent DG interior penalty methods [24]

$$\begin{aligned} &\int_{\Gamma_{\mathrm{IU}}} [\![\boldsymbol{w}_u]\!] \cdot \langle \boldsymbol{\sigma} \rangle \cdot \hat{\boldsymbol{n}}^-\, ds \rightarrow \\ &\left\{ \begin{aligned} &\int_{\Gamma_{\mathrm{IU}}} [\![\boldsymbol{w}_u]\!] \cdot \langle \boldsymbol{\sigma} \rangle \cdot \hat{\boldsymbol{n}}^-\, ds + \\ &\int_{\Gamma_{\mathrm{IU}}} \left\{ [\![\boldsymbol{u}]\!] \cdot \langle \mathbf{C} : \nabla \boldsymbol{w}_u \rangle \cdot \hat{\boldsymbol{n}}^- \right\} ds + \\ &\int_{\Gamma_{\mathrm{IU}}} \left\{ [\![\boldsymbol{w}_u]\!] \otimes \hat{\boldsymbol{n}}^- : \left\langle \frac{\beta_s}{h_s} \mathbf{C} \right\rangle : [\![\boldsymbol{u}]\!] \otimes \hat{\boldsymbol{n}}^- \right\} ds \end{aligned} \right. \end{aligned} \tag{7}$$

where $\mathbf{C}$ is the (anisotropic) elasticity tensor. In this substitution, the first term ensures the consistency of the method and is kept unchanged, the second term is the symmetrization term, which ensures the displacement compatibility and leads to an optimal convergence rate with respect to the mesh size h_s, and the third term is the quadratic stabilisation term, ensuring that the general displacement jumps are stabilised in the numerical solution. The penalty parameter β_s has to be larger than a constant that depends on the polynomial approximation for the DG interior penalty method to be stable [26, 27].

The small deformation material response is thus properly considered for the final weak formulation of the problem obtained by substituting Equations (6) and (7) into Equation (4), and which consists of finding $\boldsymbol{u}$ such that

$$\left.\begin{array}{l}\displaystyle\int_\Omega (\rho\ddot{\boldsymbol{u}}\cdot\boldsymbol{w}_u+\boldsymbol{\sigma}:\nabla\boldsymbol{w}_u)\,dv+\int_{\Gamma_{\rm IU}}[\![\boldsymbol{w}_u]\!]\cdot\langle\boldsymbol{\sigma}\rangle\cdot\hat{\boldsymbol{n}}^-\,ds+\\ \displaystyle\int_{\Gamma_{\rm IU}}\left\{[\![\boldsymbol{w}_u]\!]\otimes\hat{\boldsymbol{n}}^-:\left\langle\frac{\beta_s}{h_s}\mathbf{C}\right\rangle:[\![\boldsymbol{u}]\!]\otimes\hat{\boldsymbol{n}}^-\right\}ds+\\ \displaystyle\int_{\Gamma_{\rm IU}}\left\{[\![\boldsymbol{u}]\!]\cdot\langle\mathbf{C}:\nabla\boldsymbol{w}_u\rangle\cdot\hat{\boldsymbol{n}}^-\right\}ds+\int_{\Gamma_{\rm IC}}[\![\boldsymbol{w}_u]\!]\cdot\bar{\boldsymbol{t}}^-([\![\boldsymbol{u}]\!])\,ds=\\ \displaystyle\int_\Omega\rho\,\boldsymbol{b}\cdot\boldsymbol{w}_u\,dv+\int_{\Gamma_{\rm T}}\boldsymbol{w}_u\cdot\bar{\boldsymbol{t}}\,ds,\ \forall\ \boldsymbol{w}_u\end{array}\right\} \tag{8}$$

The weak form (8) is discretized following the finite-element method. To this end, the domain Ω is discretized into several bulk finite elements Ω^e and into several interface elements $\Gamma_{\rm I}^s$ inserted in-between these bulk elements. The displacement field $\boldsymbol{u}$ and the trial function $\boldsymbol{w}_u$ are approximated by considering the polynomial approximations

$$\boldsymbol{u}(\boldsymbol{X})=\sum_a N^a(\boldsymbol{X})\boldsymbol{u}^a\ \text{and}\ \boldsymbol{w}_u(\boldsymbol{X})=\sum_a N^a(\boldsymbol{X})\delta\boldsymbol{u}^a \tag{9}$$

where N^a is the shape function corresponding to the node a. As both the test and trial functions are discontinuous across the interface elements $\Gamma_{\rm I}^s$, the shape functions N ought to represent this discontinuity, and the degrees of freedom are thus duplicated for each bulk element comprising the node a. Considering the interface separating the two elements "minus" and "plus" as in Figure 1, the node a has the degrees of freedom $\boldsymbol{u}^{a^-}$ associated to the "minus"-element and the degrees of freedom $\boldsymbol{u}^{a^+}$ associated to the "plus"-element.

The finite-element forces are obtained by introducing the polynomial approximations (9) into the weak form (8), leading to the set of governing equations to be integrated in the time interval T:

$$\boldsymbol{M}^{ab}\ddot{\boldsymbol{u}}^b+\boldsymbol{f}^a_{\rm int}+\boldsymbol{f}^a_{\rm I}=\mathbf{f}^a_{\rm ext}\quad\forall t\in T \tag{10}$$

In this equation $\boldsymbol{M}^{ab}$ is the discretized mass matrix, $\boldsymbol{f}^a_{\rm int}$ is the internal force vector at node a, which is obtained from the elementary bulk forces following

$$\boldsymbol{f}^a_{\rm int}=\sum_e\int_{\Omega^e}\boldsymbol{\sigma}\cdot\boldsymbol{\nabla}N^a dV \tag{11}$$

$\mathbf{f}^a_{\rm ext}$ is the external force vector at node a, which is obtained from the elementary bulk forces following

$$\boldsymbol{f}^a_{\rm ext}=\sum_e\int_{\Omega^e}\rho\boldsymbol{b}N^a dV+\int_{\Gamma_{\rm T}}N^a\bar{\boldsymbol{t}}\,ds \tag{12}$$

These two force vectors are computed using classical bulk finite elements Ω^e. In this paper we use quadratic triangles integrated using 3 Gauss points.

Finally, $\boldsymbol{f}^a_{\rm I}$, the last left hand side term in Equation (10) is the interface (including the un-cracked and cracked parts of $\Gamma_{\rm I}$) force vector at node a, which is obtained from the elementary interface forces following

$$\boldsymbol{f}^{a^\pm}_{\rm I}=\begin{cases}\pm\displaystyle\sum_s\int_{\Gamma^s_{\rm IC}}\bar{\boldsymbol{t}}^-([\![\boldsymbol{u}]\!])N^{a^\pm}ds\pm\\ \displaystyle\sum_s\int_{\Gamma^s_{\rm IU}}\langle\boldsymbol{\sigma}\rangle\cdot\hat{\boldsymbol{n}}^-N^{a^\pm}ds+\\ \displaystyle\frac{1}{2}\sum_s\int_{\Gamma^s_{\rm IU}}\boldsymbol{\nabla}N^{a^\pm}\cdot\left[\left([\![\boldsymbol{u}]\!]\otimes\hat{\boldsymbol{n}}^-\right):\bar{\mathbf{C}}^\pm\right]ds\pm\\ \displaystyle\sum_s\int_{\Gamma^s_{\rm IU}}\left[\langle\frac{\beta_s}{h_s}\bar{\mathbf{C}}\rangle:[\![\boldsymbol{u}]\!]\otimes\hat{\boldsymbol{n}}^-\right]\cdot\hat{\boldsymbol{n}}^-N^{a^\pm}ds\end{cases} \tag{13}$$

This interface force vector arises from the DG/ECL formulation. It is integrated by considering an interface element $\Gamma^s_{\rm I}$ between the two "plus" and "minus" bulk elements, see Figure 1. In this work, the interface elements are quadratic lines integrated using 3 Gauss points [40]. The resulting force vector (13) has a contribution to the degrees of freedom belonging to both the "plus" and "minus" neighboring bulk elements, hence the use of the $a^\pm$ superscript and of the notation "$\pm$", which holds for "+" for the degree of freedom a^+, and for "-" for the degree of freedom a^-. In Equation (13) the shape functions $N^{a^\pm}$ are volume shape functions evaluated at the integration points of the interface elements. Due to the symmetrization terms all the nodes of the 2 neighboring bulk elements have force contributions, and not only the nodes of the common interface.

Details on the parallel implementation of the method can be found in [14, 28]. Moreover, recent works have focused on the practical implementation of the method in in-house and commercial software [29, 30].

The set of equations (10) is completed by the initial conditions $\boldsymbol{u}^a(t=0)=0$ and $\dot{\boldsymbol{u}}^a(t=0)=\boldsymbol{v}^a_0$, where $\boldsymbol{v}^a_0$ are the initial nodal velocities. The time interval of interest T is discretized into time steps and the integration is accomplished through an incremental solution procedure in each time interval $[t_n, t_{n+1}]$. To this end, an explicit time integration as the Hulbert-Chung time integration [41], which exhibits numerical dissipation, is considered. Note that due to the DG terms, the critical explicit time step is reduced by $\sqrt{\beta_s}$ [40].

What remain now to be defined are the constitutive behaviour of the bulk material, as well as the initiation and the evolution of the crack cohesive law.

2.2 Constitutive material model

In the weak form (8), the discretized Cauchy stress tensor $\boldsymbol{\sigma}$ results from the strain tensor $\boldsymbol{\varepsilon} = (1/2)(\nabla \otimes \boldsymbol{u} + \boldsymbol{u} \otimes \nabla)$ through a constitutive material law. At the nanoscale, as the grains of polySi are orthotropic in nature, anisotropic material tensor expressed in the 2D plane-stress state is used such that $\boldsymbol{\sigma} = \mathbf{C} : \boldsymbol{\varepsilon}$. At the macroscale the material is considered as homogeneous and isotropic.

2.3 Initiation of the crack

The evaluation of the stress tensor at the Gauss points of the uncracked interfaces Γ_{IU} follows previous works by Camacho and Ortiz [22], and Ortiz and Pandolfi [23]. This models the fracture in mode I, in mode II or in a combination of both using an effective stress,

$$\sigma_{\mathrm{eff}} = \begin{cases} \sqrt{(\sigma_{\mathrm{n}})^2 + (\beta)^{-2}(\tau_{\mathrm{r}})^2}, \text{if } \sigma_{\mathrm{n}} \geq 0 \\ \dfrac{1}{\beta} \ll |\tau_{\mathrm{r}}| - \mu_{\mathrm{c}} |\sigma_{\mathrm{n}}| \gg, \text{if } \sigma_{\mathrm{n}} < 0 \end{cases} \tag{14}$$

where $\beta = (K_{IIc}/K_{Ic})$ and μ_{c} are shear stress factor and friction coefficient of the material, respectively, and where the operator $\ll \bullet \gg$ is defined by

$$\ll \bullet \gg = \begin{cases} \bullet, \text{ if } \bullet \geq 0 \\ 0, \text{ if } \bullet < 0 \end{cases} \tag{15}$$

In Equation (14), $\sigma_{\mathrm{n}} = \hat{\boldsymbol{n}} \cdot \boldsymbol{\sigma} \cdot \hat{\boldsymbol{n}}$ and $\tau_{\mathrm{r}} = \sqrt{\|\boldsymbol{\sigma} \cdot \hat{\boldsymbol{n}}\|^2 - (\sigma_{\mathrm{n}})^2}$ are respectively the normal and tangential components of the surface traction at the interface. The criterion $\sigma_{\mathrm{eff}} \geq \sigma_{\mathrm{c}}$ checks the fracture onset. When it is reached at a Gauss point part of Γ_{IU}, this Gauss point becomes part of the cracked interfaces Γ_{IC} on which the extrinsic cohesive law $\bar{\boldsymbol{t}}(\llbracket \boldsymbol{u} \rrbracket)$ is integrated.

2.4 Extrinsic cohesive law

Linearly decreasing ECL, as shown in Figure 2, is considered in the present work to model the crack opening between the two fracture surfaces. As long as the ECL is monotonically decreasing, the shape of the curve does not affect the solution for brittle materials [23]. Herein $\sigma_{\mathrm{c}}, G_{\mathrm{c}}, \Delta^*$ and Δ^*_{c} are the fracture strength, critical strain energy release rate, crack tip opening displacement, and the critical crack tip opening displacement, respectively. If an unloading of the forces occurs during the crack opening, the ECL follows a reversible path connecting the origin with the unloading point on curve $(\Delta^*_{\max}, \bar{t}_{\max})$ with a straight line, where $\bar{t} = \|\bar{\boldsymbol{t}}\|$, Δ^*, and $\bar{t}_{\max}$ represent the surface traction amplitude between the crack lips, the opening of the crack, and the surface traction amplitude at the maximum crack opening $\Delta^*_{\max}$ reached during the fracture process, respectively. The critical opening displacement Δ^*_{c} is computed, as $\Delta^*_{\mathrm{c}} = [(2G_{\mathrm{c}})/\sigma_{\mathrm{c}}]$ to ensure that the correct amount of energy is released at the end of the complete fracture process.

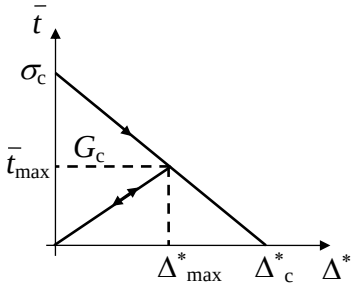

Fig. 2: Linearly decreasing extrinsic cohesive law

Once the fracture is detected at a specific interface Gauss point, the ECL is used to compute the traction vector $\bar{\boldsymbol{t}}$ between the two crack lips in terms of the effective opening displacement Δ^*. The effective opening displacement Δ^* is computed from the surface opening vector $\boldsymbol{\Delta}^*$, which is a combination of two effective openings Δ^*_{n} and Δ^*_{t} given by

$$\Delta^* = \sqrt{\ll \Delta^*_{\mathrm{n}} \gg^2 + \beta^2 (\Delta^*_{\mathrm{t}})^2} \tag{16}$$

where Δ^*_{n} and Δ^*_{t} are the separations along the normal $\hat{\boldsymbol{n}}$ and tangential $\hat{\boldsymbol{t}}$ directions, respectively, of the interface element. The computation of Δ^* is explained in details by Wu *et al.* [14]. The amplitude of the effective cohesive traction, shown in Figure 2, can then be computed by linear interpolation as

$$\bar{t} = \sigma_{\mathrm{c}} \left(1 - \tfrac{\Delta^*}{\Delta^*_{\mathrm{c}}}\right) \quad \text{for } \dot{\Delta}^* \geq 0, \text{ and } \Delta^* = \Delta^*_{\max} \tag{17}$$

$$\bar{t} = \bar{t}_{\max} \tfrac{\Delta^*}{\Delta^*_{\max}} \quad \text{for } \dot{\Delta}^* < 0, \text{ or } \Delta^* < \Delta^*_{\max} \tag{18}$$

whereas the cohesive traction vector $\bar{\boldsymbol{t}}$ can be evaluated as a function of the effective cohesive traction $\bar{t}$, following

$$\bar{\boldsymbol{t}} = \bar{t} \left(\tfrac{\Delta^*_{\mathrm{n}}}{\Delta^*} \hat{\boldsymbol{n}} + \beta \tfrac{|\Delta^*_{\mathrm{t}}|}{\Delta^*} \hat{\boldsymbol{t}} \right) \quad \text{for } \sigma_{\mathrm{n}} \geq 0 \tag{19}$$

$$\bar{\boldsymbol{t}} = \bar{t} \beta \tfrac{|\Delta^*_{\mathrm{t}}|}{\Delta^*} \hat{\boldsymbol{t}} \quad \text{for } \sigma_{\mathrm{n}} < 0 \tag{20}$$

The values of σ_{c} and G_{c} are the two minimum parameters required for the characterisation of the ECL. In this work, we will evaluate these values at the macroscopic scale, where the material is considered as isotropic and homogeneous, from the micro-scale simulations. At the microscopic scale (through mesoscopic RVEs) a method is developed accounting for the anisotropy and heterogeneity (due to the different out of plane orientation of the grains) of the polySi.

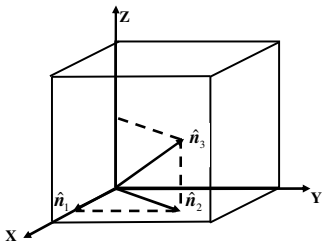

Fig. 3: Symmetry-equivalent surfaces with their normals

3 Microscale fracture of RVE model of polySi material

At first, we study RVE of polySi at the mesoscopic (microscopic) scale. A RVE consists of several grains with a completely general distribution. At the nanoscale, the constitutive material law follows a 2D plane-stress anisotropic elastic model. The 2D cohesive laws are developed to account for the anisotropic and heterogeneous nature of the polySi due to a general out-of-plane orientation of the grains. In particular as the interfaces of the finite element mesh do not follow the crystallographic planes of the Si, effective values of σ_c and G_c are at first computed for a general orientation of the interface. Secondly the weakest plane is identified over the thickness of a thin polySi film so that the correct amount of energy is released at the end of the fracture process. This allows simulating in 2D through-the-thickness fracture along weak planes not perpendicular to the film.

With a view toward the simulation of macroscale MEMS structures, the values of the resulting mesoscale effective σ_c and G_c can then be evaluated from the microscale simulations so that the crystallographic nature of the PolySi is implicitly accounted for.

As the RVEs are not rigorously representative (the number of grains considered in a RVE cannot be large enough for MEMS structures without becoming of comparable size with the macroscale) a set of realisations is considered to extract a statistical distribution of these resulting mesoscale effective values, σ_c and G_c. To be rigorous when the volume element involves fracture, it looses its representative nature and should be called micro-structural volume element [5].

The predictions are finally compared with the experimental results.

3.1 Effective fracture strength at the nano-scale

The polySi is a cubic crystal exhibiting different material properties, such as Young's modulus, Poisson ratio, fracture strength, along the crystal planes with Miller indices (1 0 0), (1 1 0), and (1 1 1), shown in Figure 3 as $\hat{\boldsymbol{n}}_1, \hat{\boldsymbol{n}}_2$, and $\hat{\boldsymbol{n}}_3$, respectively. The 2D interface (cohesive) elements, located between two bulk elements, in a discretized model are not exactly aligned with any of the crystal planes. Thus a model to compute the effective fracture strength at each interface based on the available fracture strength experimentally measured along the three possible cleavage planes (1 0 0), (1 1 0), and (1 1 1) [2, 42, 43] is required. The length of a single interface element being several times larger than the single crystal lattice spacing of polySi, the approach presented here to compute the values of effective σ_c is valid for a certain "average" direction. For a cubic crystal, the Miller indices (hkl) are normal to the surface vector $[hkl]$, i.e., Miller indices directly give the coefficients of the surface normal vector for a cubic crystal. This information provides the effective σ_c for any random orientation of a polySi grain as explained further. The same approach applies to compute the effective G_c as well.

Let $\sigma_{100}, \sigma_{110}$, and σ_{111} be the experimental values of the fracture strength that are respectively measured along the three possible cleavage planes (1 0 0), (1 1 0), and (1 1 1) [2,42,43]. The normal vectors to these planes are given as $\hat{\boldsymbol{n}}_1 = \hat{\boldsymbol{e}}_1, \hat{\boldsymbol{n}}_2 = (1/\sqrt{2})(\hat{\boldsymbol{e}}_1 + \hat{\boldsymbol{e}}_2)$, and $\hat{\boldsymbol{n}}_3 = (1/\sqrt{3})(\hat{\boldsymbol{e}}_1 + \hat{\boldsymbol{e}}_2 + \hat{\boldsymbol{e}}_3)$, respectively, where $\hat{\boldsymbol{e}}_i$ are the unit basis vectors of the global Cartesian axes as shown in Figure 3. Let there be an interface (cohesive) element, having a surface normal vector $\boldsymbol{n}$, along which σ_c has to be determined.

The surface normal vector $\boldsymbol{n}$ can be represented in the contravariant form as $\boldsymbol{n} = n^i \hat{\boldsymbol{n}}_i$, where the $\hat{\boldsymbol{n}}_i$ are treated as the local basis vectors. As the vectors $\hat{\boldsymbol{n}}_1, \hat{\boldsymbol{n}}_2$, and $\hat{\boldsymbol{n}}_3$ are not orthogonal to one another, their dual vectors are computed at first. The total volume contained within the local basis vectors is

$$v = (\hat{\boldsymbol{n}}_1 \times \hat{\boldsymbol{n}}_2) \cdot \hat{\boldsymbol{n}}_3 \Rightarrow v = \frac{1}{\sqrt{6}} \tag{21}$$

The dual basis vectors are then computed as

$$\left.\begin{aligned} &\boldsymbol{n}^1 = \left[\frac{\hat{\boldsymbol{n}}_2 \times \hat{\boldsymbol{n}}_3}{v}\right] \Rightarrow \boldsymbol{n}^1 = \hat{\boldsymbol{e}}_1 - \hat{\boldsymbol{e}}_2 \\ &\boldsymbol{n}^2 = \sqrt{2}\left(\hat{\boldsymbol{e}}_2 - \hat{\boldsymbol{e}}_3\right), \text{ and } \boldsymbol{n}^3 = \sqrt{3}\,\hat{\boldsymbol{e}}_3 \end{aligned}\right\} \tag{22}$$

such that $\boldsymbol{n}_i \cdot \boldsymbol{n}^j = \delta_i^j$ is satisfied. The projection of $\boldsymbol{n}$ in the dual basis vectors is given as

$$n^{100} = \boldsymbol{n} \cdot \boldsymbol{n}^1,\ n^{110} = \boldsymbol{n} \cdot \boldsymbol{n}^2,\ n^{111} = \boldsymbol{n} \cdot \boldsymbol{n}^3 \tag{23}$$

Therefore, the effective fracture strength vector $\boldsymbol{\sigma}_c$ along $\boldsymbol{n}$ can be constructed as

$$\left.\begin{aligned} &\boldsymbol{\sigma}_c = \sigma_{100}\, n^{100}\, \hat{\boldsymbol{n}}_1 + \sigma_{110}\, n^{110}\, \hat{\boldsymbol{n}}_2 + \sigma_{111}\, n^{111}\, \hat{\boldsymbol{n}}_3 \Rightarrow \\ &\boldsymbol{\sigma}_c = \left(\sigma_{100}\, n^{100} + \frac{\sigma_{110}\, n^{110}}{\sqrt{2}} + \frac{\sigma_{111}\, n^{111}}{\sqrt{3}}\right) \hat{\boldsymbol{e}}_1 + \\ &\qquad \left(\frac{\sigma_{110}\, n^{110}}{\sqrt{2}} + \frac{\sigma_{111}\, n^{111}}{\sqrt{3}}\right) \hat{\boldsymbol{e}}_2 + \left(\frac{\sigma_{111}\, n^{111}}{\sqrt{3}}\right) \hat{\boldsymbol{e}}_3 \end{aligned}\right\} \tag{24}$$

The magnitude σ_c of $\boldsymbol{\sigma}_c$ is thus given as

$$\sigma_c = \sqrt{\left(\sigma_{100}\, n^{100} + \frac{\sigma_{110}\, n^{110}}{\sqrt{2}} + \frac{\sigma_{111}\, n^{111}}{\sqrt{3}}\right)^2 + \left(\frac{\sigma_{110}\, n^{110}}{\sqrt{2}} + \frac{\sigma_{111}\, n^{111}}{\sqrt{3}}\right)^2 + \left(\frac{\sigma_{111}\, n^{111}}{\sqrt{3}}\right)^2} \tag{25}$$

This equation is applicable only when $\boldsymbol{n}$ is in between the solid angle formed by $\hat{\boldsymbol{n}}_1, \hat{\boldsymbol{n}}_2$, and $\hat{\boldsymbol{n}}_3$, where these are the surface normal vectors corresponding to the orientation planes (1 0 0), (1 1 0), and (1 1 1), respectively, which may not always be true. The symmetry property of the cubic crystal is used to enable the applicability of Equation (25) for any orientation of $\boldsymbol{n}$. Due to the symmetry of the cubic crystal, there are 26 symmetry planes distributed in 8 quadrants as

$$\left.\begin{aligned} \{100\} &= (100),(010),(001),(\bar{1}00),(0\bar{1}0),(00\bar{1}) \\ \{110\} &= (110),(\bar{1}10),(\bar{1}\bar{1}0),(1\bar{1}0),(011),(0\bar{1}1), \\ &\quad (0\bar{1}\bar{1}),(101),(10\bar{1}),(\bar{1}0\bar{1}),(\bar{1}01),(01\bar{1}) \\ \{111\} &= (111),(\bar{1}11),(\bar{1}\bar{1}1),(1\bar{1}1),(11\bar{1}),(\bar{1}1\bar{1}), \\ &\quad (\bar{1}\bar{1}\bar{1}),(1\bar{1}\bar{1}) \end{aligned}\right\} \tag{26}$$

The magnitude of the fracture strength is equal along all the planes within each family of planes $\{100\}, \{110\}$, and $\{111\}$. These symmetry planes (26) give a total of 48 sets of solid angles (6 solid angles per quadrant). This information is used while determining the correct solid angle in which the vector $\boldsymbol{n}$ lies. At first, each set of solid angles is considered, and the corresponding dual basis vectors are computed. The vector $\boldsymbol{n}$ is then projected in these dual basis vectors. If all the projections are ≥ 0 for a specific solid angle it is concluded that the vector $\boldsymbol{n}$ lies within this solid angle formed by the set of 3 corresponding surface normal vectors. Finally, the correctly identified set of the surface normal vectors is used while computing the effective σ_c along the plane normal to the vector $\boldsymbol{n}$, as given in Equation (25). In order to test the correctness of Equation (25), the Cartesian coordinates of $\boldsymbol{n}$ are constructed by the polar coordinates (by progressively increasing the angles $\theta \in [0, 2\pi]$ and $\phi \in [0, \pi]$), and the corresponding effective σ_c is computed by Equation (25). The results are presented in Figure 4 for specific values $\sigma_{100} = 1.53$, $\sigma_{110} = 1.21$, and $\sigma_{111} = 0.87$ GPa of a single crystal silicon [2, 42, 43]. It can be seen that the effective σ_c passes through the three values used along the symmetry planes with the symmetric distribution in all the 8 quadrants of a unit length cubic crystal, which is an expected result. This model is also applied to compute the effective G_c along the interface plane with surface normal $\boldsymbol{n}$ as shown in Figure 5.

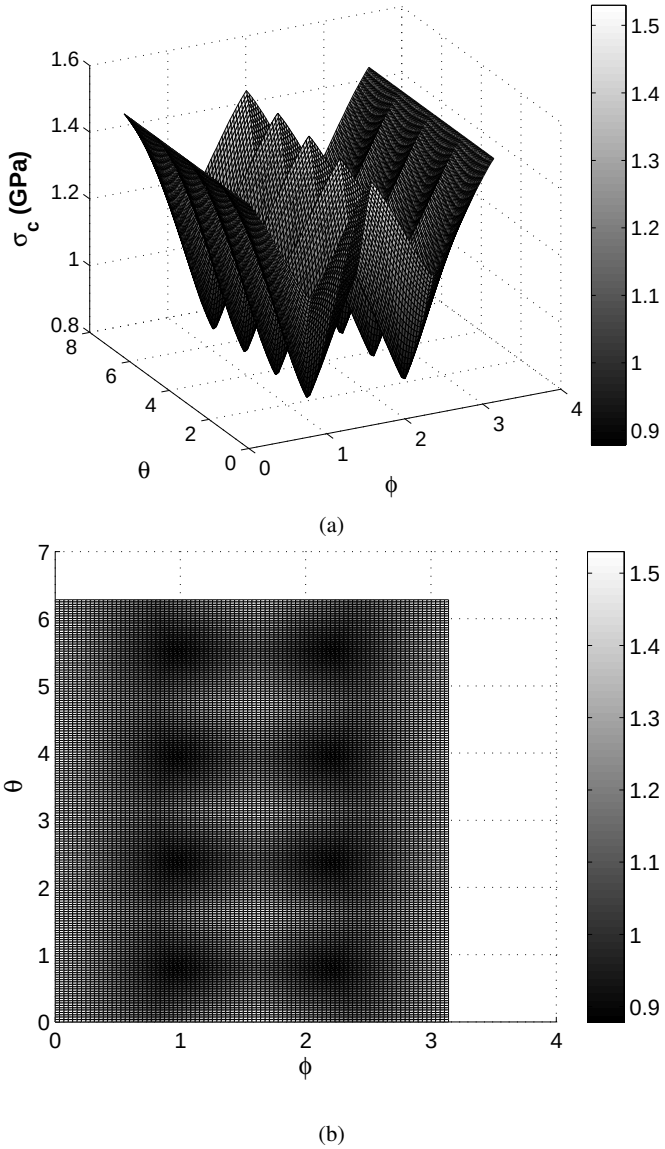

Fig. 4: Distribution of σ_c within a unit cube of polySi

3.2 Thickness effect

The fracture process of a thin polySi film is modelled using 2D plane-stress conditions, thus the surface normal vector $\hat{\boldsymbol{n}}$ of the cohesive element always lies in the plane. Nonetheless, the fracture surface normal $\boldsymbol{n}$ may be oriented with a certain angle with respect to the thickness of the film, where the effective value of σ_c could be lower as compared with the plane-stress situation. This leads to a weakest crystal plane not necessarily perpendicular to the film. Furthermore, several grains can be along the thickness of a thin polySi film. This 3D nature of the problem is then taken into account following the approach described in Figure 6.

Let us assume an interface (cohesive) element, and let $\hat{\boldsymbol{t}}, \hat{\boldsymbol{t}}_0$, and $\hat{\boldsymbol{n}}$ be the in-plane surface tangent, out-of-plane surface normal vectors, and cohesive element normal, respectively, as shown in Figure 6. These 3 vectors form a set of local basis vectors, and the Cauchy stress tensor $\boldsymbol{\sigma}$ is represented in terms of these local basis vectors. This interface

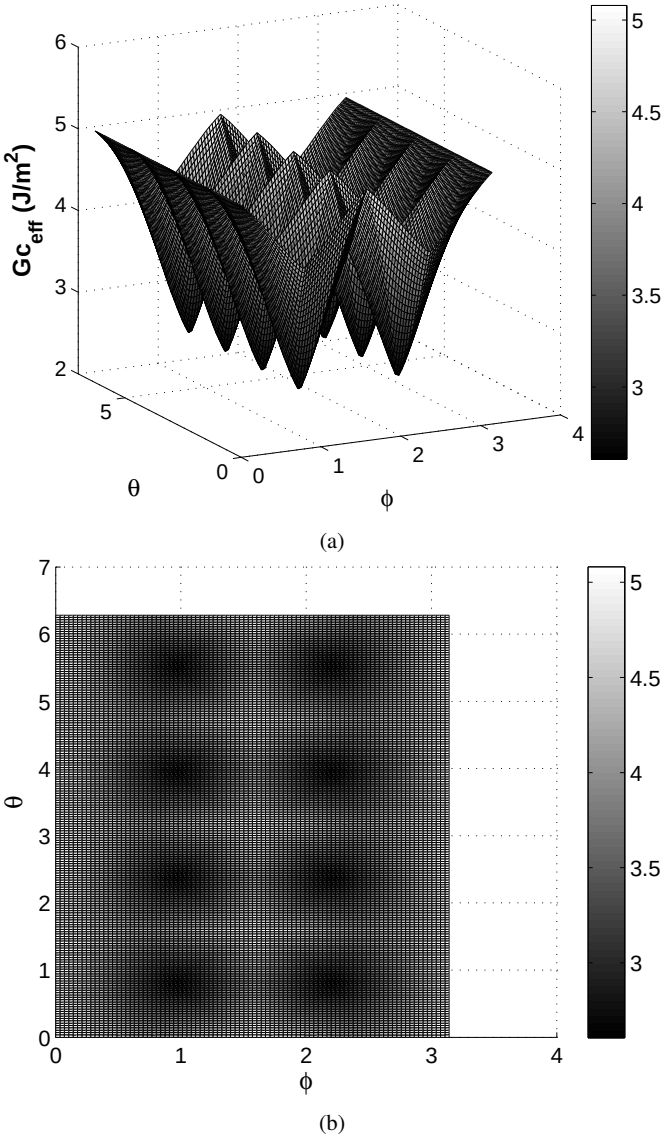

Fig. 5: Distribution of G_c within a unit cube of polySi

element is now rotated by an angle θ around $\hat{\boldsymbol{t}}$. Thus, the local basis vectors transform to $\hat{\boldsymbol{t}}^{'}, \hat{\boldsymbol{t}}_0^{'}$, and $\hat{\boldsymbol{n}}^{'}$, respectively. The transformation equations are given as

$$\left.\begin{aligned} \hat{\boldsymbol{n}}^{'} &= \cos(\theta)\,\hat{\boldsymbol{n}} + \sin(\theta)\,\hat{\boldsymbol{t}}_0 \\ \hat{\boldsymbol{t}}^{'} &= \hat{\boldsymbol{t}} \\ \hat{\boldsymbol{t}}_0^{'} &= -\sin(\theta)\,\hat{\boldsymbol{n}} + \cos(\theta)\,\hat{\boldsymbol{t}}_0 \end{aligned}\right\} \tag{27}$$

The Cauchy stress tensor $\boldsymbol{\sigma}$ is already available along the interface element. Also the effective values of $\sigma_c(\theta)$ and $G_{c\text{eff}}(\theta)$ are computed in the direction $\hat{\boldsymbol{n}}^{'}$, as explained in Section 3.1. Now, the magnitudes of the stresses acting on

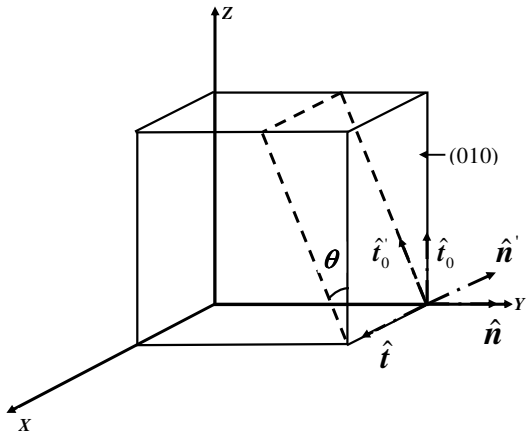

Fig. 6: Rotation of an interface element along the thickness of the thin polySi film, where $\hat{\boldsymbol{n}}$ is shown along Y axis for an illustration purpose.

the rotated plane are computed from $\boldsymbol{\sigma}$ and $\hat{\boldsymbol{n}}^{'}, \hat{\boldsymbol{t}}_0^{'}$, and $\hat{\boldsymbol{t}}^{'}$ as

$$\left.\begin{aligned} &\sigma_n = (\boldsymbol{\sigma}\hat{\boldsymbol{n}}^{'})\cdot\hat{\boldsymbol{n}}^{'}, \tau = (\boldsymbol{\sigma}\hat{\boldsymbol{n}}^{'})\cdot\hat{\boldsymbol{t}}^{'}, \tau_0 = (\boldsymbol{\sigma}\hat{\boldsymbol{n}}^{'})\cdot\hat{\boldsymbol{t}}_0^{'} \\ &\tau_r = \sqrt{(\tau)^2 + (\tau_0)^2} \end{aligned}\right\} \tag{28}$$

The effective stress $\sigma_{\text{eff}}(\theta)$ along the rotated plane is computed from σ_n and τ_r using Equation (14). The $\sigma_c(\theta), G_c(\theta)$, and $\sigma_{\text{eff}}(\theta)$ are computed with θ varying from -90 to + 90^0 with a fixed increment to check whether the fracture criterion $\sigma_{\text{eff}}(\theta) \geq \sigma_c(\theta)$ is satisfied. This $\sigma_{\text{eff}}(\theta)$ value is used to compute the maximum effective crack tip opening $\Delta_c^*(\theta) = (2\,G_c(\theta)/\sigma_{\text{eff}}(\theta))$. The in-plane crack tip opening is computed as $\Delta_c^* = \{\Delta_c^*(\theta)/\cos(\theta)\}$, such that the correct amount of energy is released by the ECL method. The $\sigma_{\text{eff}}(\theta)$ value corresponding to $\theta = 0$ is used in the cohesive law, shown in Figure 2, as a starting point $(\Delta^* = 0, \sigma_c)$ in order to maintain the continuity of the distribution of the stress field between the unfractured and fractured stages.

3.3 Results and discussion

The simulation of the fracture of a tensile test performed on a thin polySi film RVE is performed on aas follows. At first, a model of a thin polySi film is developed by Voronoï tessellation with each Voronoï polygon treated as a grain. The size of each grain is approximately maintained equal to 100 nm, and a random orientation (random Euler angles) is assigned as shown in Figure 7a. However, the preferential orientations as experimentally observed can also be assigned as demonstrated in Section 3.3.2. The dimensions of the model are chosen as to ensure a stable fracture process, i.e., the total strain energy stored in a body should be less than or equal to the total fracture energy required to be released. The following approach has been followed to satisfy

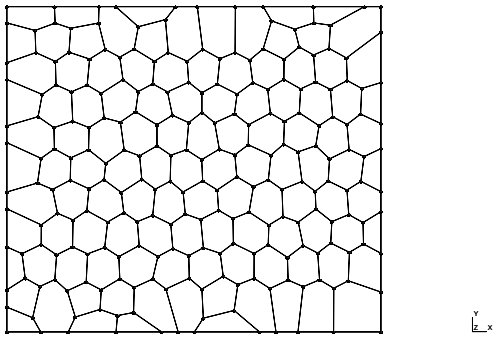

(a)

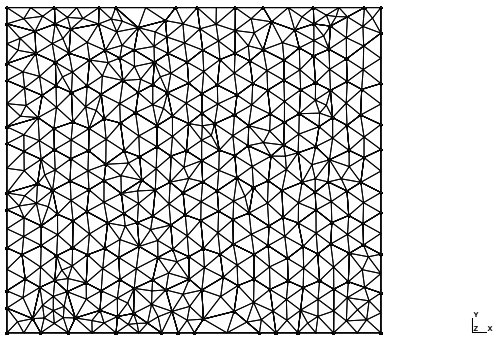

(b)

Fig. 7: A representative volume element model of a thin polySi film with (a) 112 grains and (b) a mesh containing 874 elements

this requirement. At first, the dimensions of the model are fixed with certain length l, height h and thickness t, and one sample simulation is performed by an appropriate value of the load step that approximately gives a quasi static loading. Based on the mesoscopic stress vs strain plot obtained at the end of the simulation, the correct length of the model is computed by $l \leq (G_c/(0.5\,\sigma_c\,\varepsilon_c))$, where G_c, σ_c and ε_c are the critical strain energy release rate, obtained fracture stress and strain, respectively. The model is then regenerated with this new value of length l to approximately ensure that the stable through-the-thickness fracture is obtained. The final dimensions of the model are $l = 1.15, h = 1$ and $t = 0.05$ μm. The typical finite element mesh size is decided with reference to the smallest edge of the grains present in a model as shown in Figure 7b. This ensures that at least one element is present along the grain boundaries, see Figure 7b. Experimentally, the fracture strength of a single crystal silicon is highly affected by the micro-machining process and the silicon etchant used, thus a wide variation is observed in its value [2, 42]. It is difficult to exactly incorporate the actual surface roughness of a polySi film in the present simulation. The standard values for typical silicon crystals produced by the standard micro-machining process are used in the present study.

The values of fracture strength along the (1 0 0), (1 1 0) and (1 1 1) orientation planes for the single crystal silicon are used as $\sigma_{100} = 1.53, \sigma_{110} = 1.21$ and $\sigma_{111} = 0.87$ GPa [2, 42, 43], respectively. The values of G_c are similarly used as $G_{c\,100} = 5.08, G_{c\,110} = 4.2$ and $G_{c\,111} = 2.56$ J/m^2, [44, 45], respectively[1]. In order to ensure that the fracture is preferably detected at a single location at the beginning, the computed value of the effective fracture strength at a specific Gauss point along the interface element is varied within ± 10 %. The anisotropic material model in each grain has a cubic symmetry, with as material parameters in the (1 0 0) direction a Young's modulus $E = 144$ GPa, a Poisson ratio $\nu = 0.28$, and a shear modulus $\mu = 80$ GPa [2, 42, 43, 46]. The value of the density is $\rho = 2.33$ g/cm^3.

This model is loaded in uniaxial tension as in the experiments. The force (computed) and displacement (applied) values along the loading edge are archived. The dynamic explicit time integration is performed to ensure convergence, and the value of the load step is decided to ensure that a quasi-static regime is achieved. As soon as a fracture is detected at any Gauss point along an interface element, the monotonically decreasing linear ECL is applied to compute the stress. The interface elements are present at two locations, viz. within a grain and along the grain boundaries. The fracture strength and effective stress along the interface elements, that are present within a grain, are computed as explained in Sections 3.1 and 3.2, respectively. The value of the fracture strength along the interface elements, that are present along the grain boundaries, is assigned corresponding to the (1 0 0) orientation, and the effective stress is computed without the thickness effect. This adopted approach in the present work is based on the experimentally observed fact that the polySi mainly undergoes the transgranular fracture, so the grain boundaries are stronger than the grains.

In order to capture the spread of fracture strength associated to the probabilistic orientation of grains, 10 different sets of the fracture results are obtained with each time new Euler angles assigned to the grains. For each of the 10 sets, a mesoscopic ECL is extracted from the microscopic force vs. displacement plot [9, 14], as $u^M = u^m - [(l/E)\,(f^m/(ht)]$ where f^m, u^m and u^M are the microscopic force, displacement and macroscopic displacement, respectively, and E is the slope of microscopic stress vs. strain plot till the fracture stress is reached. The mean and standard deviation of the macroscopic effective crack tip opening displacement Δ^* and fracture stress σ_c are computed based on the 10 sets of the extracted mesoscopic ECL from the simulation results. An average mesoscopic cohesive law is thus developed that incorporates the statistical variation of σ_c and Δ^*. This is

[1] These units are modified in the simulation setup to avoid bad conditioning numbers

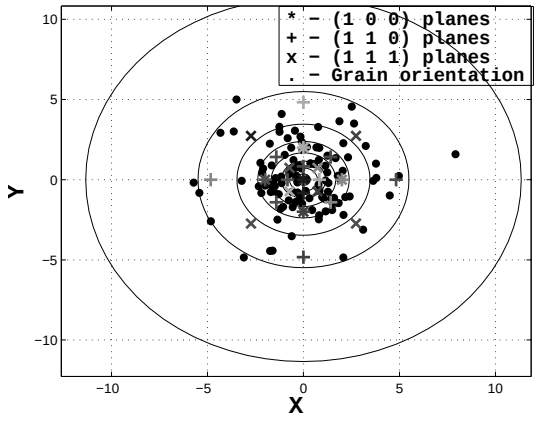

Fig. 8: Stereographic projection of the surface normal of the orientation of grains without any average preferred orientation

first conducted for a general distribution of the grain orientation before considering the case of preferred orientation.

3.3.1 Fracture of a thin polySi film RVE without preferred grain orientation

Different sets (10) of the fracture results are now obtained for this model by each time assigning a random out-of-plane orientation to the grains. The results from one of the sets are provided here for reference. The random out-of-plane orientation of 112 different grains is shown by the stereographic projection of the surface normal of their orientations in Figure 8. There is no preferential out-of-plane orientation in this case.

The mesoscopic stress vs. strain plot is shown in Figure 9a, and the extracted mesoscopic cohesive law is shown in Figure 9b. The external load steps could be seen in Figure 9a for the pre-fracture state that are caused by the dynamic effects. A smooth loading can be obtained by further reducing the time step. The through-the-thickness fracture is shown in Figure 10. It is also seen in Figure 10 that the crack is initiated at both ends of the polySi RVE. This could be explained by the fact that no notches are present along the edges, so there is an equal probability of the crack occurring at several places, along the height of the model, at the same time. The more important aspects are that both cracks finally meet, and that fracture is transgranular. Few elements could be disturbed during the crack propagation, as there is no stress concentration at the onset of crack so the fracture may be detected at more than one Gauss point along the interface elements belonging to the same bulk element.

The effective $G_c = (0.5\,\Delta_c^*\,\sigma_c)$ is computed by the mesoscopic cohesive law given in Figure 9b and obtained as $G_c = 2.97$ J/m^2, where $\Delta_c^* = 5.6 \times 10^{-3}$ μm and $\sigma_c = 1.0$ GPa.

The results obtained by all the 10 simulated sets are analysed, as explained above, and one mesoscopic cohesive law

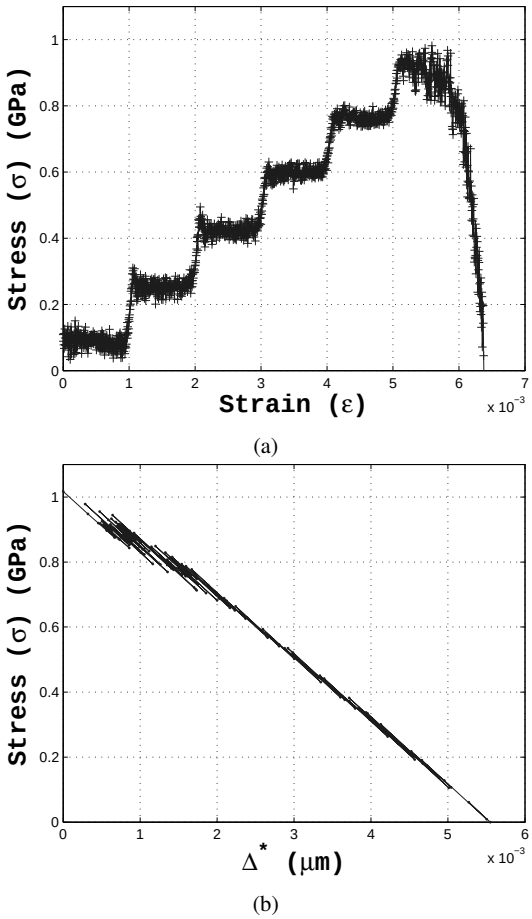

Fig. 9: (a) Stress vs. strain evolution of the RVE, (b) mesoscopic cohesive law when the grains in the polySi film are assigned a random orientation

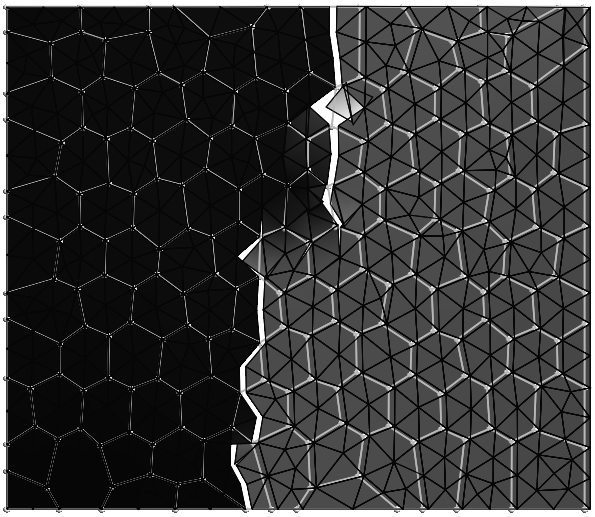

Fig. 10: Crack path when the grains in the polySi film are assigned a random orientation

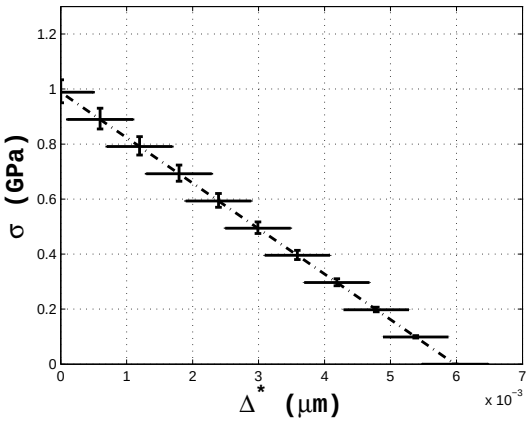

Fig. 11: Average macroscopic extrinsic cohesive law

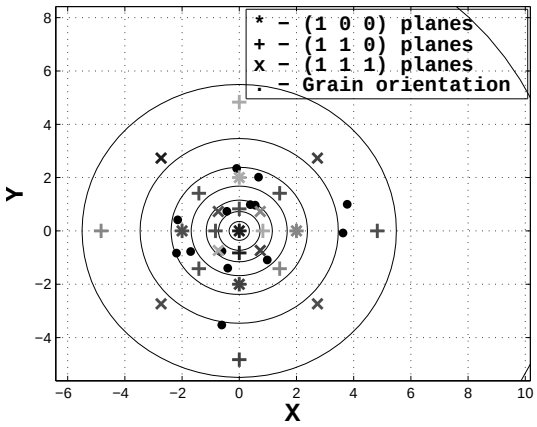

Fig. 12: Stereographic projection of the surface normal of the out-of-plane orientation of the grains that are involved in the fracture process shown in Figure 10, where an average preferred orientation is in between (1 1 0) and (1 1 1)

is extracted for each realisation. Because of the random nature of the grain orientation, each realisation leads to the different values of σ_c and G_c. The values of mean $\bar{\sigma}_c$ and standard deviation σ_{σ_c} of σ_c are computed as

$$\bar{\sigma}_c = \frac{1}{n}\sum_{i=1}^{n}(\sigma_c)_i,\ \ \sigma_{\sigma_c} = \sqrt{\frac{1}{(n-1)}\sum_{i=1}^{n}[(\sigma_c)_i - \bar{\sigma}_c]^2} \qquad (29)$$

where $n = 10$ is our samples number. The values of mean $\bar{\Delta}_c^*$ and standard deviation $\sigma_{\Delta_c^*}$ of Δ_c^* are also computed similarly. These values are obtained as $\bar{\sigma}_c = 0.99$ GPa and $\sigma_{\sigma_c} = 4.04\times10^{-2}$ GPa, and $\bar{\Delta}_c^* = 5.98\times10^{-3}$ μm and $\sigma_{\Delta_c^*} = 4.96\times10^{-4}$ μm. The average mesoscopic cohesive law is thus developed based on these values as shown in Figure 11. It is worth mentioning these values are linked with the size of the polySi RVE, and will change with a change in the size of the RVE. In this paper, we assume that a size of the RVE comparable to the size of the finite elements that will be used at the macroscale is meaningful [47,48]. A more evolved analysis should account for the correlation distance [49].

All the simulation results at the microscopic level show that the first fracture always occurs at the value of effective stress $\sigma_{\text{eff}}(\theta)$, as explained in Section 3.2, in between the fracture strengths along the (1 1 0) and (1 1 1) orientation planes. This means that, irrespective of the orientation of grains, there will be at least one interface element whose surface normal will be closely aligned, due to the thickness effect, to the normal of the (1 1 1) orientation plane. This implies that the crack will always propagate in the average direction of the (1 1 1) orientation plane. This is clearly seen in Figure 12, where the stereographic projection is given only for the grains that are involved in the fracture process where an average preferred out of plane orientation is in-between the (1 1 0) and (1 1 1) orientations. A similar behaviour has also been experimentally observed [45]. The average value of $G_c \approx 2.96$ J/m^2 is also between the values corresponding to the (1 1 0) and (1 1 1) orientation planes. All the results at the microscopic level have different crack paths, as

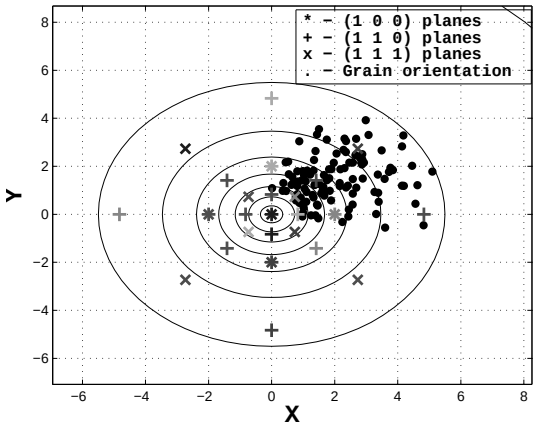

Fig. 13: Stereographic projection of the surface normal of the orientation of grains with an average (1 1 0) orientation

each time different out of plane orientation is assigned to the grains. The orientation of grains thus affects the crack path, while may not drastically affect the fracture stress at which the crack initiation is detected.

3.3.2 Fracture of a highly textured thin polySi film RVE with all grain orientations close to (1 1 0)

This section contains the simulation results when all the grains in Figure 7a are assigned an out-of-plane orientation close to (1 1 0) plane. The objective of this simulation is to make comparisons with several experimental results in the open literature, as well as in-house experiments performed as explained later. The average (1 1 0) orientation of grains is shown by their stereographic projection in Figure 13. The microscopic stress vs. strain plot and the mesoscopic cohesive law are shown in Figures 14a and 14b, respectively, and the crack path is shown in Figure 15. The value of effec-

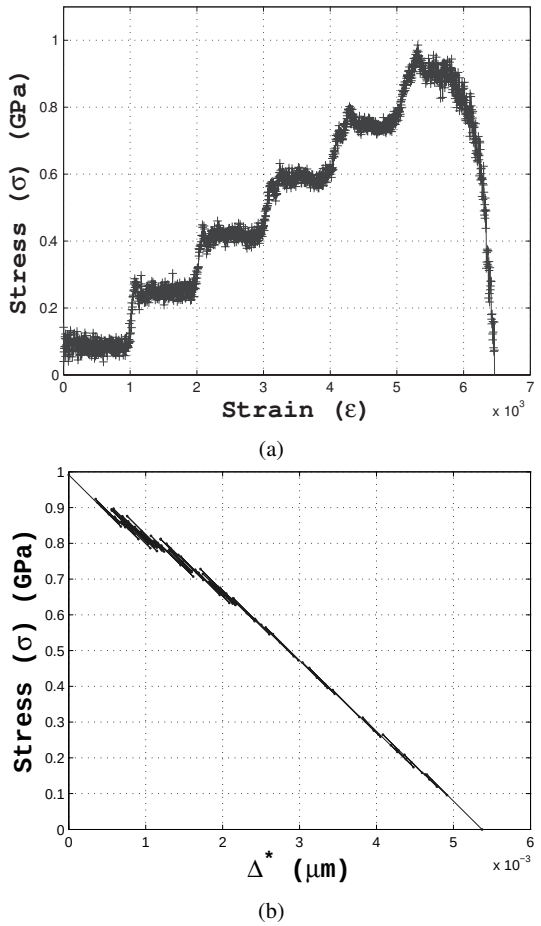

Fig. 14: (a) Stress vs. strain plot, (b) mesoscopic cohesive law for an average out-of-plane (1 1 0) grain orientation

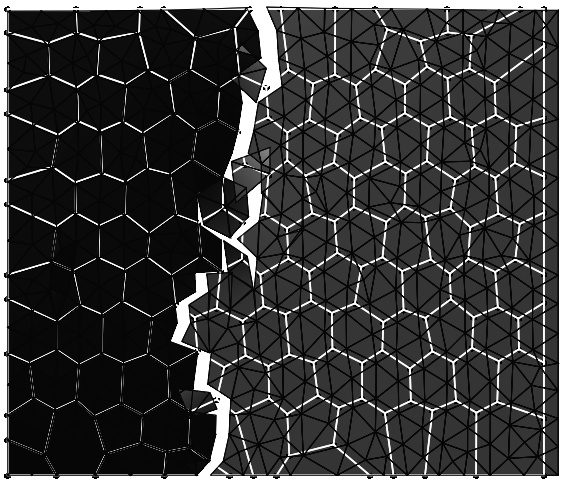

Fig. 15: Crack path for an average out-of-plane (1 1 0) grain orientation

tive G_c is computed by the cohesive law as well as by the energy balance as equal to 2.77 and 3.0 J/m^2, respectively. These values are approximated as they are computed by assuming a complete mode-I fracture, such that the fracture surface area is assumed to be a normal cross-section $(h \times t)$. The crack path shows that the actual fracture surface is not exactly along the normal cross-section.

The overall fracture strength is equal to $\sigma_c \approx 1.0$ GPa, which is close to the average value obtained by Yi *et al.* [42] but slightly lower than the input value $\sigma_{110} = 1.21$ GPa for a single crystal silicon with a preferred (1 1 0) out-of-plane orientation. The reason behind this was explained at the end of Section 3.3.1. The present results closely match with Suwito *et al.* [2] for <1 1 0> silicon T-structures having sharp 90^o corner at the point of the reduction of cross-sectional area. This is an important test case as it mimics the actual transitions occuring in the micromechanical structures. The value of fracture strain is $\varepsilon_c \approx 0.56\%$, which is very close to the average value obtained by Sato *et al.* [43] for a single crystal silicon film having <1 1 0> preferred orientation.

3.4 Experimental observations

The micro-structure and the roughness of a thin polySi film have been experimentally analysed, in the context of this research, to have a consistent comparison between the experiment and simulation results. For these experiments, a 240 nm-thick polySi layer has been deposited on top of an oxidised Si substrate. In order to extract the Young's modulus as well as the fracture strain of the deposited polySi layer, on-chip tensile test structures have been manufactured. The principle and process of the preparation of samples are elaborated in [34–39]. During the tensile test there are no longer interactions between the substrate and the film.

Automated crystallographic orientation mapping in a transmission electron microscope (ACOM - TEM) is a newly developed technique attached to TEM, which is used in the present work to determine the local orientation of polySi grains. The electron diffraction (ED) patterns, in place of Kikuchi patterns, are collected with an external charge coupled digital (CCD) camera. The acquired ED pattern is then stored in a computer and compared (off-line) with the precalculated templates and the best match is selected [50]. The experimental measurements were performed by Philips CM20 operating at 200 kV and equipped with a LaB6 gun and an external source device, DigiSTAR (R) developed by NanoMEGAS for ACOM-TEM experiments [50]. Figure 16 shows ACOM-TEM orientation mapping recorded by a 20 nm step size and an acquisition frequency of around 100 frames per second for all the sample surface analysis. In order to increase the quality of the orientation map and to highlight the micro-structure of the sample, the step size was de-

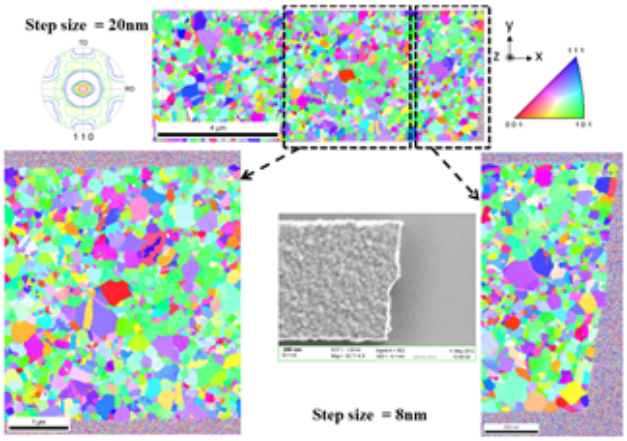

Fig. 16: Top view of the out-of-plane orientation map of a 240 nm-thick and 4 μm-wide polySi sample. Orientation maps of 20 and 8 nm as step size and 111 pole figure.

creased to 8 nm and 60 frames per second. The average grain size is estimated to be $\approx$ 110 nm with a standard deviation of 90 nm. The large standard deviation is due to the log-normal distribution of the grain size. The micro-structure is composed of a large number of small grains with a size smaller than 100 nm and also few larger grains characterised by a diameter larger than 500 nm. The sample exhibits a preferential (110) out-of-plane fiber texture and no specific in-plane orientation is emerged, as seen in Figure 16. The manufactured samples are thus comparable to the the RVEs studied in the previous section.

The scanning electron microscope (SEM) observation of the sidewall shows the presence of one or two grains through the thickness (Figure 17a) as used in the simulated geometry (Section 3.2). Concerning the fracture process, the crack path appears to be clearly transgranular, as shown in Figure 17b, which is in good agreement with our numerical studies. The fracture strain extracted from this test structure is 0.96% ($\pm$ 0.07%). It corresponds to a fracture stress of about 1.41 GPa ($\pm$ 0.1) for Young's modulus of 147 GPa [34]. These values are higher than the ones obtained in Section 3.2. This can be explained by the different preparation process compared to the experiments in references [2, 42, 43] used to calibrate σ_{100}, σ_{110}, and σ_{111} of our numerical model.

The fracture of a brittle polySi film is initiated from critical flaws located along the external surfaces, i.e., the sidewalls, top and bottom surfaces [51]. These flaws are generated by the micromachining processes during the sample preparation. They might be microstructural defects as grain boundary grooves that emerge on external surfaces and/or geometrical imperfections directly generated by the preparation process, as shown in Figure 17a. The nature and location of the critical flaws depend on the preparation process and on the sample thickness, as their micro-structure is

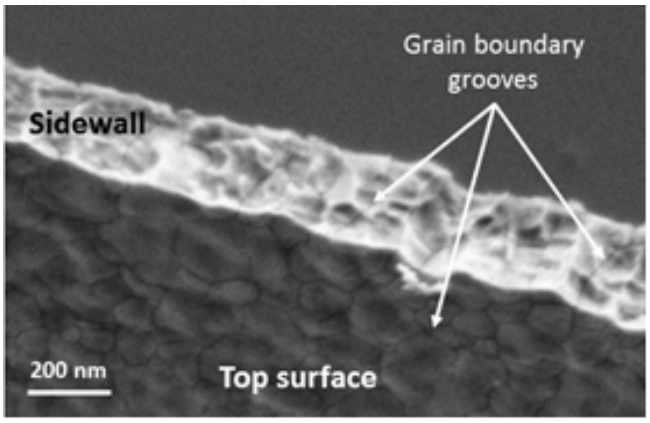

(a)

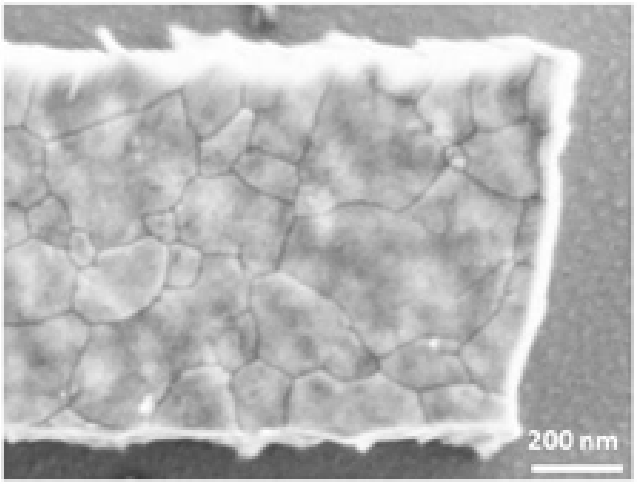

(b)

Fig. 17: (a) SEM image of the sidewall of the 240 nm-thick polySi sample, (b) SEM image of the top view of fracture zone for 900 nm-wide polySi sample

governed by both. The fracture is initiated at the flaw corresponding to the highest stress concentration which is governed by several factors, such as the morphology, density, size of the flaw, local grain orientation, local fracture toughness, and the local residual stress state. In this specific case, the sidewall roughness appears larger than that of the top and bottom surfaces. Thus, the critical flaws are most probably located on the sidewalls. Nevertheless, although the grain boundary grooves emerge on the sidewalls and are visible, it is not possible to precisely conclude that they constitute the critical flaws for the initiation of the fracture. More in-depth studies of the effect of sidewall roughness on the fracture behaviour of thin polySi films have to be performed to identify and characterise the population of the main critical flaws.

These results could be used to prepare an accurate modelling of the MEMS fracture process. As a first step, in the

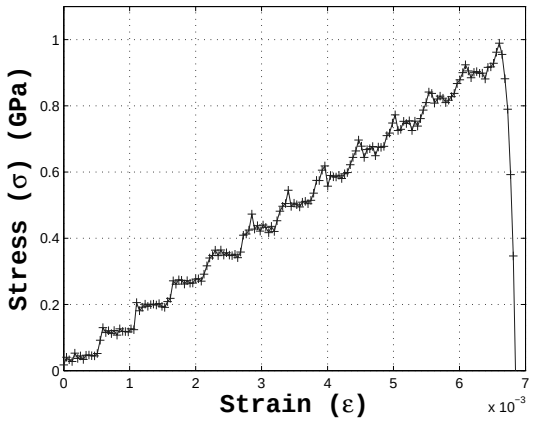

(a)

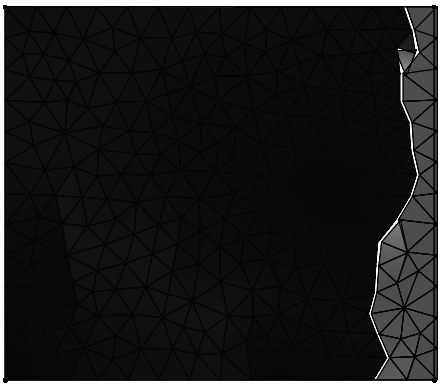

(b)

Fig. 18: (a) Stress vs. strain plot, (b) complete fracture of a thin polySi film at the macroscopic level for the model discretized by 504 finite elements

next section we will study a macro-structure in which the flaws are modelled by a notch.

4 Fracture of a thin polySi film at the macroscopic level

In this section, a new model of the thin polySi film is chosen to perform the simulation at the macroscopic or MEMS length scale where the domain of the model is treated as a continuum, i.e., without the explicit discretization of the underlying micro-structure. The average mesoscopic cohesive law given in Figure 11 is imposed, for the Gauss points where the fracture is detected, by specifying the values of σ_c and G_c at each node within their lower and upper limits obtained from the RVE simulations conducted in the previous Section. This ECL is implemented by randomly assigning the σ_c and G_c bounded by their lower and upper limits (obtained in Section 3.3.1) at each Gauss point, such that the critical crack tip opening displacement Δ_c^* is automatically bounded by its lower and upper limits. Thus $\sigma_c^- = 0.948, \sigma_c^+ = 1.03$ GPa, and $G_c{}^- = 2.8297, G_c{}^+ = 2.955$ J/m^2 values are used such that $(\Delta_c^*)^- = 5.5\times10^{-3}, (\Delta_c^*)^+ = 6.5\times10^{-3}$ μm values are obtained.

The simulations at the macroscopic scale implicitly assume that the underlying micro-structure of the MEMS is closely represented by the RVE at the mesoscopic length scale, such that the statistical variation of the fracture strength obtained by the RVE closely represents the actual scenario at the MEMS length scale. This is achieved firstly without considering any defect, and secondly with considering an edge defect at the centre of the length l of a thin polySi film.

4.1 Fracture of a thin polySi film without notch at the macroscopic level

A new model is considered with $l = 3.45, h = 3$ and $t = 0.05$ μm at the macroscopic length scale. This model is discretized such that the size of the finite elements is approximately equal to the size of the RVE considered in Section 3.3.1. The results of the simulation are as follows. The stress vs. strain plot and the fracture are shown in Figure 18. The total surface or fracture energy for this model $U_{\text{surf}} \approx (3.0 \times 0.05 \times 3 \times 10^{-6}) \approx 4.5\times10^{-1}$ J is well achieved at the end of the fracture. The fracture in the present case is unstable, evident from Figure 18a, as the total strain energy U_{int} at the beginning of the fracture is much higher than the required fracture energy.

In order to test the correctness of the mesoscopic cohesive law as well as DG/ECL framework implementation, the length l is modified, such that the stable fracture is obtained, as explained in Section 3.3. The values of σ_c and ε_c are taken from Figure 18a and an average $G_c = 2.9$ N/m^2 is used to compute the new length $l \approx 0.9$ μm. The new model is built again and simulated with all the parameters as before. The simulation results show that a prefect stable mode-I fracture is obtained and all the vital values are correctly recovered. The stress vs. strain plot and the cohesive law are given in Figure 19, and the complete mode-I fracture is given in Figure 20. The total potential energy at the end of fracture is $U_{\text{pot}} = 4.2\times10^{-1}$ J, which gives $G_c = 2.8$ J/m^2 for a normal cross-section (3.0×0.05) μm^2. The total area under the cohesive law also equals to $G_c = 2.8$ J/m^2. The maximum internal strain energy $U_{\text{int}} = 4.37\times10^{-1}$ J, which is close to the total required fracture energy $U_{\text{surf}} = 4.5\times10^{-1}$ J, results in a stable crack propagation.

4.2 Fracture of a thin polySi film with an edge defect at the macroscopic level

All the simulation results presented so far correspond to the geometry of a thin polySi film with smooth edges. In reality, several defects (notches) are generated along the edges

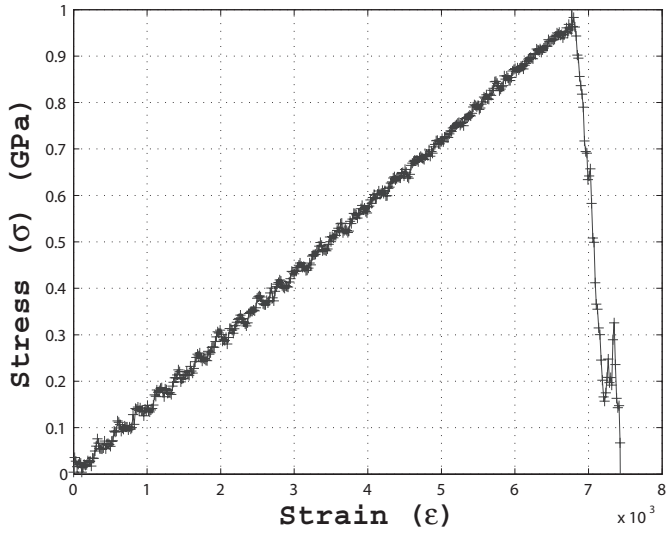

(a)

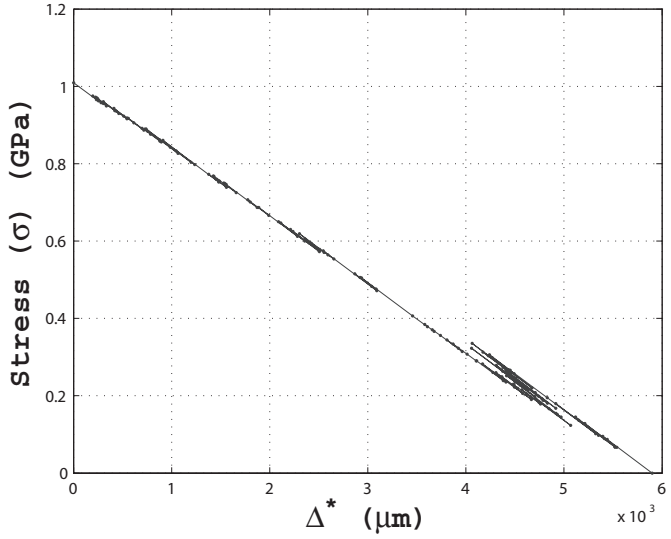

(b)

Fig. 19: (a) Stress vs. strain plot, (b) global cohesive law of a thin polySi film for the stable crack propagation at the macroscopic level

of MEMS due to the micromachining process, thus considerably affecting the fracture behaviour of MEMS. Therefore it is pertinent to study such a model of a polySi film having at least one edge defect.

The macroscopic model from Section 4.1 is modified at first and a defect in the form of a small notch is created at the centre of a top edge, such that the height at the centre became $h_c = 2.52\,\mu$m. The simulation is performed keeping all the parameters as before. Figures 18a and 21a show that the fracture stress (computed from the reaction force and from the MEMS section at the notch part in the second case) is reduced by at least 20% due to the presence of the defect. The obtained crack path can also be physically observed as

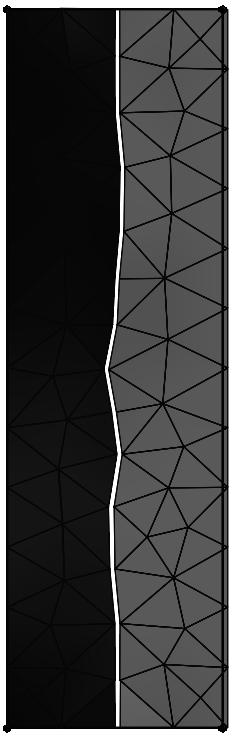

Fig. 20: Complete mode-I fracture for the stable crack propagation at the macroscopic level

there will be a stress concentration at the tip of a notch. As the U_{pot} is much higher than U_{surf}, the fracture is unstable.

Secondly, the length of the model is further increased to $l = 23.0\,\mu$m to have a more realistic size and discretized with a much larger number of finite elements without changing any other parameters, such that the size of the elements is approximately equal to the size of RVE in Section 3.3.1. It is purposefully avoided to have a refined mesh in the central region to have a more general simulation results without any influence of the mesh density. The stress vs. strain plot and fracture are shown in Figure 22. The stress concentration at the tip of the defect is reduced due to a decrease in the notch angle (the stress is computed from the reaction force and from the MEMS section at the notch part), thus resulting in a slightly higher value of the fracture stress in Figure 22a as compared with Figure 21a.

5 Conclusions

The fracture of a thin polySi film has been simulated by a 2-scale approach.

At the lower scale, the mesoscale RVEs are studied in which the grains are explicitly meshed. In order to apply the cohesive zone method, a novel model to compute the effective fracture strength σ_c of an anisotropic material along

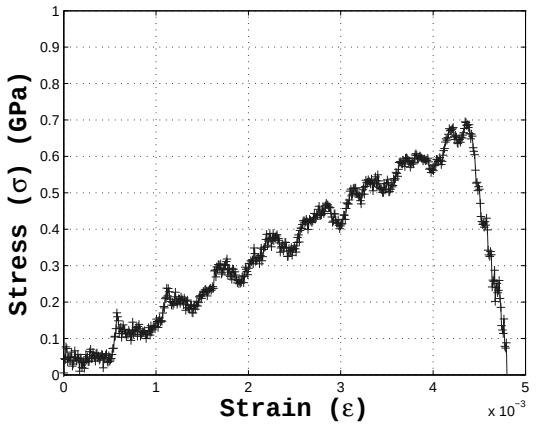

(a)

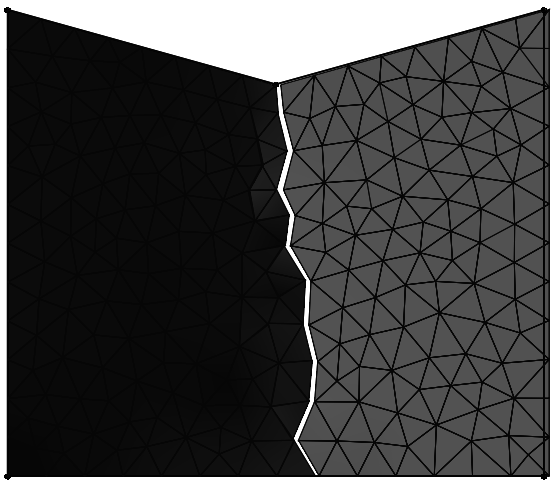

(b)

Fig. 21: (a) Stress vs. strain plot, and (b) complete fracture of a polySi film, having a notch, at the macroscopic level

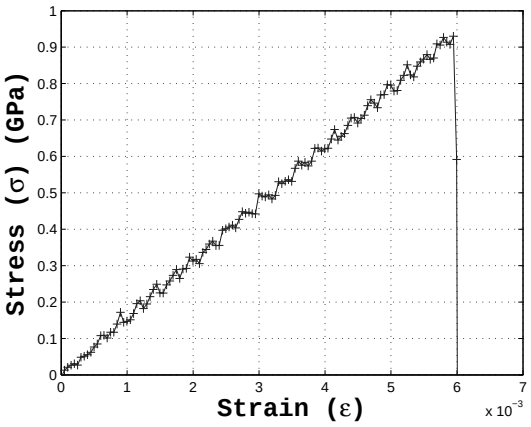

(a)

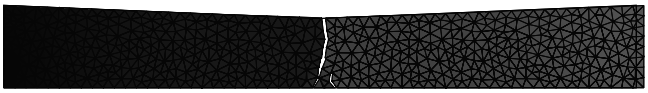

(b)

Fig. 22: (a) Stress vs. strain plot, and (b) complete fracture of a thin polySi film having $l = 23$ μm at the macroscopic level

arbitrary interfaces is proposed, which also satisfies the symmetry requirement of the unit cube of silicium. In order to use 2D simulations, the thickness effect is accounted for by allowing a through-the-thickness fracture to occur along arbitrary orientation planes. The results obtained by the numerical simulations are broadly in accordance with the experimentally observed fact that irrespective of the orientation of crystals, a crack eventually occurs and propagates along an approximately (1 1 1) cleavage plane, as the surface energy of this orientation plane is smaller than the (1 0 0) and (1 1 0) planes. The simulation of a uniaxial loading of a thin polySi film at the mesoscopic level results in the fracture stress and strain of ≈ 1.0 GPa and 0.6%, respectively, and $G_c \approx 3.0$ J/m^2. All these values are between the values corresponding to the out-of-plane grain orientations (1 1 0) and (1 1 1). This means that, the fracture is always propagated along the weakest cohesive element with an out-of-plane orientation close to the orientation of (1 1 0) or (1 1 1) planes.

From the RVEs studied, a mesososcopic cohesive law can be extracted to be used as an input for the macroscale simulations. As the RVEs are not rigorously representative (the number of grains considered in a RVE cannot be large enough for MEMS structures without becoming of comparable size with the macroscale) a set of realisations is considered to extract a statistical distribution of these resulting mesoscale effective values, σ_c and G_c. At the macroscale, the polySi film at the MEMS length scale can thus be studied as a homogeneous isotropic continuum, which reduces the computational resources.

The fracture simulations at both scales are achieved using the combined DG/ECL method. In this framework the interface (cohesive) elements are inserted between the bulk elements from the beginning of the simulation itself. As the ECL is activated only at the interface where the effective stress reaches the fracture strength, the method remains consistent. Moreover no *a priori* knowledge of crack path as well as the remeshing of the geometry are required. This advantage of the suggested framework allows the scalable parallelization of the code.

The fracture of a polySi thin film is experimentally performed in-house by the on-chip fracture test, with (1 1 0) average local preferential orientation of the sample in the out-of-plane direction. The in-plane orientations are random, but based on the symmetry-equivalent cleavage planes, (1 0 0)

and (1 1 0) orientations influence the fracture behaviour of this particular sample of polySi. The values of fracture strain and stress are found to be 0.96% ($\pm$ 0.07%) and 1.41 GPa ($\pm$ 0.1) with this setup. Thus the fracture stress, as predicted, is between the fracture strengths along the (1 0 0) and (1 1 0) cleavage planes. The comparison between the simulations and in-house experiments show that the fracture stress obtained by the simulations is close to, but slightly lower than, the experimental values. This can be explained by the different preparation process than for the experiments considered to calibrate σ_{100}, σ_{110}, and σ_{111} of our numerical model. The crack path of the fracture is found to be transgranular by both the experiments and simulations. The present work can be extended in the future by studying and incorporating the influence of the side wall roughness and other flaws on the fracture behaviour of a polySi film.

Acknowledgements The authors gratefully acknowledge the financial support from F. R. S. - F. N. R. S. under the project number FRFC 2.4508.11 as well as under the project PDR T.0122.13 "MECANO".
The support of the Belgian Science Policy through the IAP 7/21 project is gratefully acknowledged.
Computational resources have been provided by the supercomputing facilities of the "Consortium des Équipements de Calcul Intensif en Fédération Wallonie Bruxelles (CÉCI)" funded by the "Fond de la Recherche Scientifique de Belgique (FRS-FNRS)".

References

1. F.W. DelRio, M.L. Dunn, B.L. Boyce, A.D. Corwin, M.P. De Boer, Journal of Applied Physics **99**(10), 104304 (2006)
2. W. Suwito, M.L. Dunn, S.J. Cunningham, D.T. Read, Journal of Applied Physics **85**(7), 3519 (1999)
3. J. Sharpe, W.N., K. Turner, R. Edwards, Experimental Mechanics **39**(3), 162 (1999)
4. W. Sharpe, K.M. Jackson, K. Hemker, Z. Xie, Microelectromechanical Systems, Journal of **10**(3), 317 (2001)
5. E. Coenen, V. Kouznetsova, E. Bosco, M. Geers, International Journal of Fracture **178**(1-2), 157 (2012). DOI 10.1007/s10704-012-9765-4
6. V.P. Nguyen, O. Lloberas-Valls, M. Stroeven, L.J. Sluys, International Journal for Numerical Methods in Engineering **89**(2), 192 (2012). DOI 10.1002/nme.3237
7. B.C.N. Mercatoris, T.J. Massart, International Journal for Numerical Methods in Engineering **85**(9), 1177 (2011). DOI 10.1002/nme.3018
8. T. Belytschko, S. Loehnert, J.H. Song, International Journal for Numerical Methods in Engineering **73**(6), 869 (2008). DOI 10.1002/nme.2156
9. C.V. Verhoosel, J.J.C. Remmers, M.A. Gutiérrez, R. de Borst, International Journal for Numerical Methods in Engineering **83**(8-9), 1155 (2010)
10. S. Tang, A. Kopacz, S. Chan O´ Keeffe, G.B. Olson, W. Liu, Computational Mechanics **52**(6), 1265 (2013). DOI 10.1007/s00466-013-0874-3
11. S. Tang, A.M. Kopacz, S.C. O´ Keeffe, G.B. Olson, W.K. Liu, Journal of the Mechanics and Physics of Solids **61**(11), 2108 (2013). DOI 10.1016/j.jmps.2013.07.007
12. P. Kerfriden, O. Goury, T. Rabczuk, S. Bordas, Computer Methods in Applied Mechanics and Engineering **256**(0), 169 (2013). DOI 10.1016/j.cma.2012.12.004
13. M. Holl, S. Loehnert, P. Wriggers, International Journal for Numerical Methods in Engineering **93**(1), 23 (2013). DOI 10.1002/nme.4373
14. L. Wu, D. Tjahjanto, G. Becker, A. Makradi, A. Jèrusalem, L. Noels, Engineering Fracture Mechanics **104**(0), 162 (2013)
15. D.S. Dugdale, Journal of the Mechanics and Physics of Solids **8**(2), 100 (1960)
16. G.I. Barenblatt, (Elsevier, 1962), pp. 55–129. DOI 10.1016/S0065-2156(08)70121-2
17. N. Moës, J. Dolbow, T. Belytschko, International Journal for Numerical Methods in Engineering **46**(1), 131 (1999). DOI 10.1002/(SICI)1097-0207(19990910)46:1$<$131::AID-NME726$>$3.0.CO;2-J
18. N. Moës, T. Belytschko, Engineering Fracture Mechanics **69**(7), 813 (2002). DOI 10.1016/S0013-7944(01)00128-X
19. F. Armero, C. Linder, International Journal of Fracture **160**, 119 (2009). DOI 10.1007/s10704-009-9413-9
20. R. de Borst, M.A. Gutiérrez, G.N. Wells, J.J.C. Remmers, H. Askes, International Journal for Numerical Methods in Engineering **60**(1), 289 (2004). DOI 10.1002/nme.963
21. A. Hillerborg, M. Modéer, P.E. Petersson, Cement and Concrete Research **6**(6), 773 (1976)
22. G.T. Camacho, M. Ortiz, International Journal of Solids and Structures **33**(20-22), 2899 (1996)
23. M. Ortiz, A. Pandolfi, International Journal for Numerical Methods in Engineering **44**(9), 1267 (1999)
24. L. Noels, R. Radovitzky, International Journal for Numerical Methods in Engineering **68**(1), 64 (2006)
25. J. Mergheim, E. Kuhl, P. Steinmann, Communications in Numerical Methods in Engineering **20**(7), 511 (2004)
26. R. Radovitzky, A. Seagraves, M. Tupek, L. Noels, Computer Methods in Applied Mechanics and Engineering **200**, 326 (2011). DOI 10.1016/j.cma.2010.08.014
27. G. Becker, C. Geuzaine, L. Noels, Computer Methods in Applied Mechanics and Engineering **200**(45-46), 3223 (2011)
28. G. Becker, L. Noels, International Journal for Numerical Methods in Engineering **93**(1), 80 (2013)
29. Y. Charles, Finite Elements in Analysis and Design **88**(0), 55 (2014). DOI 10.1016/j.finel.2014.05.008
30. V.P. Nguyen, Engineering Fracture Mechanics (0), (2014). DOI 10.1016/j.engfracmech.2014.07.003
31. S. Greek, F. Ericson, S. Johansson, M. FÃijrtsch, A. Rump, Journal of Micromechanics and Microengineering **9**(3), 245 (1999)
32. W.N. Sharpe, B. Yuan, R. Vaidyanathan, R.L. Edwards, in *Microlithography and Metrology in Micromachining II*, *Society of Photo-Optical Instrumentation Engineers (SPIE) Conference Series*, vol. 2880 (1996), *Society of Photo-Optical Instrumentation Engineers (SPIE) Conference Series*, vol. 2880, pp. 78–91
33. W. Van Arsdell, S. Brown, Microelectromechanical Systems, Journal of **8**(3), 319 (1999)
34. S. Gravier, M. Coulombier, A. Safi, N. Andre, A. Boe, J.P. Raskin, T. Pardoen, Microelectromechanical Systems, Journal of **18**(3), 555 (2009)
35. E. Escobedo-Cousin, S.H. Olsen, T. Pardoen, U. Bhaskar, J.P. Raskin, Applied Physics Letters **99**(24), 241906 (2011)
36. U. Bhaskar, V. Passi, S. Houri, E. Escobedo-Cousin, S.H. Olsen, T. Pardoen, J.P. Raskin, Journal of Materials Research **27**(03), 571 (2012)
37. V. Passi, U. Bhaskar, T. Pardoen, U. Sodervall, B. Nilsson, G. Petersson, M. Hagberg, J.P. Raskin, Microelectromechanical Systems, Journal of **21**(4), 822 (2012)
38. F. Ureña, S.H. Olsen, L. Šiller, U. Bhaskar, T. Pardoen, J.P. Raskin, Journal of Applied Physics **112**(11), 114506 (2012)
39. U. Kumar Bhaskar, T. Pardoen, V. Passi, J.P. Raskin, Applied Physics Letters **102**(3), 031911 (2013)
40. L. Noels, R. Radovitzky, International Journal for Numerical Methods in Engineering **74**(9), 1393 (2008). DOI 10.1002/nme.2213

41. G.M. Hulbert, J. Chung, Computer Methods in Applied Mechanics and Engineering **137**(2), 175 (1996). DOI 10.1016/S0045-7825(96)01036-5
42. T. Yi, L. Li, C.J. Kim, Sensors and Actuators A: Physical **83**(1-3), 172 (2000)
43. K. Sato, T. Yoshioka, T. Ando, M. Shikida, T. Kawabata, Sensors and Actuators A: Physical **70**(1-2), 148 (1998)
44. J.J. Gilman, Journal of Applied Physics **31**(12), 2208 (1960)
45. C. Messmer, J.C. Bilello, Journal of Applied Physics **52**(7), 4623 (1981)
46. M. Hopcroft, W. Nix, T. Kenny, Microelectromechanical Systems, Journal of **19**(2), 229 (2010)
47. K. Alzebdeh, M. Ostoja-Starzewski, Probabilistic Engineering Mechanics **11**(4), 205 (1996)
48. M. Ostoja-Starzewski, International Journal of Solids and Structures **35**(19), 2429 (1998)
49. V. Lucas, L. Wu, M. Arnst, G. Jean-Claude, S. Paquay, V.D. Nguyen, L. Noels, in *Proceedings of the 9th International Conference on Structural Dynamics, EURODYN 2014*, ed. by A. Cunha, E. Caetano, P. Ribeiro, G. Müller (2014), pp. 2691–2698
50. M. Galceran, A. Albou, K. Renard, M. Coulombier, P. Jacques, S. Godet, Microscopy and Microanalysis **19**(03), 693 (2013)
51. T. Tsuchiya, O. Tabata, J. Sakata, Y. Taga, in *Micro Electro Mechanical Systems, 1997. MEMS '97, Proceedings, IEEE., Tenth Annual International Workshop on* (1997), pp. 529–534